Cell

A plant immune protein enables broad antitumor response by rescuing microRNA deficiency

Graphical abstract

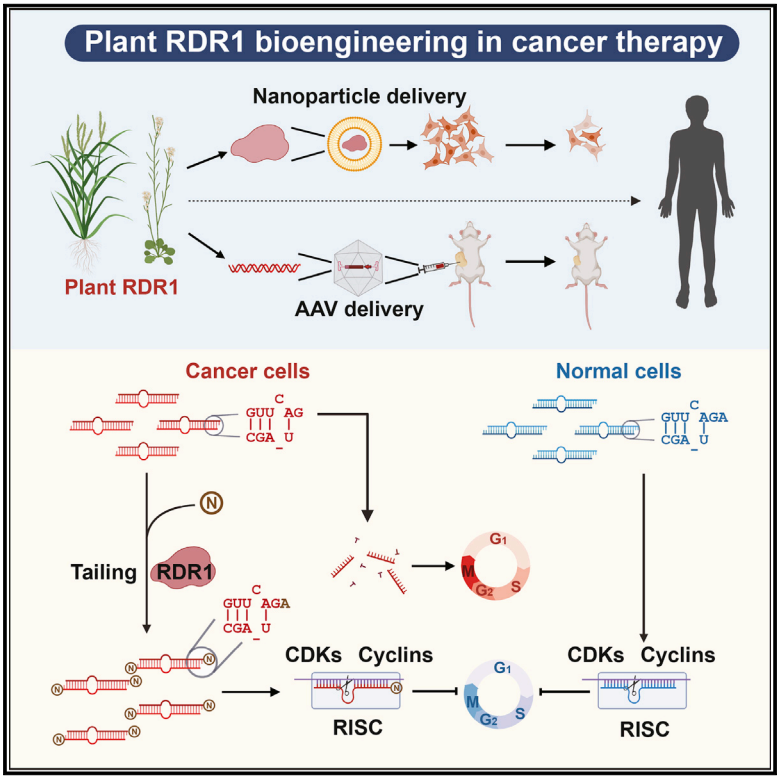

Highlights

- RDR1 protein broadly inhibits cancer cell proliferation by targeting cell cycle
- Unusual miRNA isoforms with 1-nt-shorter 3′ ends are accumulated in different tumors
- RDR1 repairs problematic miRNA isoforms in cancer by adding mononucleotides
- RDR1 suppresses growth of multiple types of solid tumors and leukemias in mice

Authors

Ye Qi, Li Ding, Siwen Zhang, ..., Yi Li, Hong Wu, Peng Du

Correspondence

pengdu@pku.edu.cn

In brief

miRNA isoforms with 1-nt-shorter 3′ ends, which cannot be efficiently associated with the AGO2 complex, are accumulated in different human primary cancer samples and cancer cell lines. Ectopic expression of plant-RNA-dependent RNA polymerase 1, which is able to modify these AGO2-free miRNA duplex isoforms with mononucleotides to eventually rescue the defective miRNA pathway, specifically blocks cell cycle in both solid cancers and leukemias.

Qi et al., 2022, Cell *185*, 1888–1904
May 26, 2022
https://doi.org/10.1016/j.cell.2022.04.030

CellPress

CellPress

Cell

Article

A plant immune protein enables broad antitumor response by rescuing microRNA deficiency

Ye Qi,[1,2,4] Li Ding,[1,4] Siwen Zhang,[1,2] Shengze Yao,[3] Jennie Ong,[1,2] Yi Li,[3] Hong Wu,[1,2] and Peng Du[1,2,5,*]

[1]MOE Key Laboratory of Cell Proliferation and Differentiation, School of Life Sciences, Peking University, Beijing 100871, China

[2]Peking-Tsinghua Center for Life Sciences, Academy for Advanced Interdisciplinary Studies, Peking University, Beijing 100871, China

[3]The State Key Laboratory of Protein and Plant Gene Research, School of Life Sciences, Peking University, Beijing 100871, China

[4]These authors contributed equally

[5]Lead contact

*Correspondence: pengdu@pku.edu.cn

https://doi.org/10.1016/j.cell.2022.04.030

SUMMARY

Cancer cells are featured with uncontrollable activation of cell cycle, and microRNA deficiency drives tumorigenesis. The RNA-dependent RNA polymerase (RDR) is essential for small-RNA-mediated immune response in plants but is absent in vertebrates. Here, we show that ectopic expression of plant RDR1 can generally inhibit cancer cell proliferation. In many human primary tumors, abnormal microRNA isoforms with 1-nt-shorter 3′ ends are widely accumulated. RDR1 with nucleotidyltransferase activity can recognize and modify the problematic AGO2-free microRNA duplexes with mononucleotides to restore their 2 nt overhang structure, which eventually rescues AGO2-loading efficiency and elevates global miRNA expression to inhibit cancer cell-cycle specifically. The broad antitumor effects of RDR1, which can be delivered by an adeno-associated virus, are visualized in multiple xenograft tumor models *in vivo*. Altogether, we reveal the widespread accumulation of aberrant microRNA isoforms in tumors and develop a plant RDR1-mediated antitumor stratagem by editing and repairing defective microRNAs.

INTRODUCTION

Aberrant activation of cell cycle and proliferation is indispensable for tumorigenesis (Hanahan and Weinberg, 2011; Otto and Sicinski, 2017). Cell cycle is well-organized and precisely regulated by complexes containing cyclins, cyclin-dependent kinases (CDKs), and checkpoint proteins in normal tissues. The dysregulation of upstream mitogenic signaling pathways and direct mutations of cell-cycle genes cause unscheduled overactivation of cell cycle, which eventually result in tumorigenesis (Malumbres and Barbacid, 2009; Otto and Sicinski, 2017). Although cell-cycle inhibitors have been developed, the related toxicological effects and drug resistance are still huge challenges for clinical applications (Suski et al., 2021).

RNA interference (RNAi) refers to a type of small RNA-mediated post-transcriptional regulation (Bernstein et al., 2001; Fire et al., 1998; Meister and Tuschl, 2004; Zamore et al., 2000). Small RNAs mainly include microRNAs (miRNAs) and small interfering RNA (siRNAs). In mammals, primary miRNAs (pri-miRNA) with stem-loop structures are cleaved twice by DROSHA/DGCR8 complex, followed by DICER (ribonuclease III) protein, and generate mature miRNA duplexes with 2 nt 3′ end overhang, which are then recognized by and loaded into Argonaute (AGO) proteins to form functional RNA-induced silencing complexes (RISCs) (Bartel, 2018; Denli et al., 2004; Gregory et al., 2004; Hammond et al., 2000; Lee et al., 2003). miRNA terminal modifications mediated by terminal nucleotidyltransferases (such as TUTases) have been widely identified and play important roles in RISC recognition, miRNA stabilization, degradation, and target repression (Sheu-Gruttadauria et al., 2019; Thornton et al., 2014; Tu et al., 2015; Yu and Kim, 2020).

miRNAs are indispensable for various physiological activities, and many miRNAs are known to target and suppress cell-cycle genes to directly control cell proliferation (Bueno and Malumbres, 2011; Hydbring et al., 2017). miRNA dysregulation or deficiency, such as global miRNA dosage decrease, has been widely reported to cause human cancer (Gaur et al., 2007; Lambo et al., 2019; Lin and Gregory, 2015; Lu et al., 2005; Ramírez-Moya et al., 2019; Sun et al., 2016; Thomson et al., 2006; Walz et al., 2015). However, the universal features of miRNA isoforms in primary tumors and cancer cells have not been systematically characterized, which is crucial to mechanically understand miRNA deficiency in different cancers.

Different from miRNAs, siRNAs are derived from double-stranded RNA (dsRNA) substrates that are synthesized by different RNA-dependent RNA polymerases (RDRs). RDRs

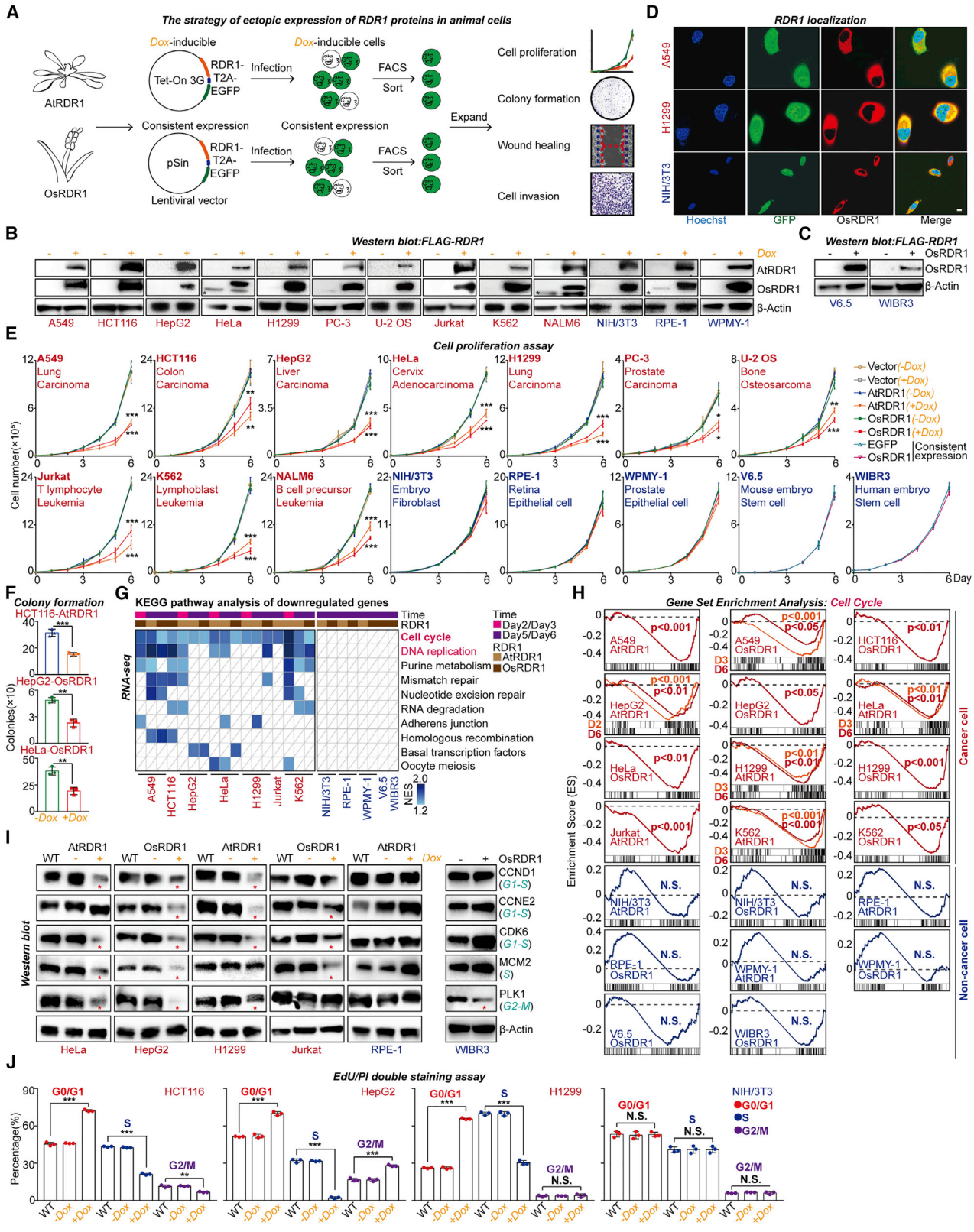

(legend on next page)

have been identified in almost all eukaryotes but are lost in vertebrates with cell-based secondary immune systems during evolution (Zong et al., 2009). In plants, RDR1-dependent siRNAs especially participate in antiviral immune response (Cao et al., 2014; Du et al., 2011; Guo et al., 2019; Moazed, 2009). In recent years, cross-species bioengineering has been successfully applied in basic research and translational medicine, such as CRISPR-Cas from bacteria (Cong et al., 2013; Jinek et al., 2012; Mali et al., 2013; Sharma et al., 2021). We therefore propose to perform plant RDR1-based bioengineering in mammals and to further investigate its potential translational medicine applications.

In this study, we successfully expressed RDR1 protein from *Arabidopsis thaliana* (At) and *Oryza sativa* (Os) in mammalian cells, which profoundly inhibited cell proliferation of all 10 different cancer cell lines tested but had not affected 5 non-cancer cell lines. Interestingly, we found that plant RDR1 can globally increase miRNA expression in different cancer cells and that miRNA pathway is indispensable for RDR1 to target cell-cycle genes and repress cancer cell proliferation. Unexpectedly, we found that abnormal miRNA isoforms with 1-nt-shorter 3′ ends, which are poorly associated with AGO2, are widely accumulated in many different primary tumors and cancer cell lines, but not in healthy tissues. Plant RDR1 with nucleotidyltransferase activity is able to recognize and modify such AGO2-free miRNA duplex isoforms with mononucleotides to restore the regular 2 nt overhang structure of miRNA duplexes and elevate their loading efficiency into AGO2, which eventually increases global miRNA expression and re-activates the deficient miRNA pathway in cancer cells. By contrast, loss of the nucleotidyltransferase activity eliminates the effects of RDR1 on miRNA expression, cell-cycle repression, and tumor growth inhibition. In different xenograft tumor models, we prove that RDR1 dramatically inhibits growth of both solid and blood cancers *in vivo*. Finally, through nanoparticles and adeno-associated viruses (AAVs), we realized RDR1 delivery in cancer cell lines and in xenograft model, respectively. In summary, our study uncovers abnormal accumulation of 1-nt-shorter miRNA isoforms widely in various human primary tumors, which provides insights into understanding the global miRNA dosage reduction during tumorigenesis. Using plant immune protein RDR1, we build a broad antitumor reaction by rescuing miRNA deficiency in cancer cells and develop a stratagem to edit and manipulate miRNAs as a powerful weapon to fight against human diseases such as cancer.

RESULTS

Ectopic expression of plant immune protein RDR1 specifically represses cancer cell proliferation

To perform plant RDR1-based bioengineering in mammalian cells, we cloned RDR1 genes from At and Os, separately, into lentiviral vectors carrying a co-expressed EGFP gene, which were then used to infect different mammalian cells. Eventually, we obtained 13 stable RDR1-inducible cell lines including 7 solid tumors (A549, HCT116, HepG2, HeLa, H1299, PC-3, and U-2 OS), 3 leukemia (Jurkat, K562 and NALM6) and 3 non-cancer somatic cell lines (NIH/3T3, RPE-1, and WPMY-1), as well as two embryonic stem cell lines (mouse V6.5 and human WIBR3) with consistent RDR1 expression (Figures 1A and S1A). Expression of AtRDR1 and OsRDR1 proteins in all the above cell lines were verified by western blot (Figures 1B and 1C). Furthermore, by using the lentiviral vector expressing mCherry-fused OsRDR1 protein, we observed that OsRDR1 protein was clearly localized in the cytoplasm but not in the nucleus (Figure 1D).

Very surprisingly and unexpectedly, we found that AtRDR1 and OsRDR1 were both able to significantly repress proliferation of all 10 cancer cell lines tested but had no impact on all other 5 non-cancer cells (Figure 1E). RDR1 can also dramatically suppress colony formation ability of HCT116, HepG2, and HeLa cells (Figures 1F and S1B). Moreover, wound-healing and cell invasion assays on A549 and H1299 cells suggested that plant RDR1 obviously blocked cancer cell migration and invasion (Figures S1C and S1D).

Plant RDR1 generally suppresses cell-cycle process in different cancer cells

Molecularly, RNA sequencing (RNA-seq)-based gene set enrichment analyses (GSEA) suggest that both AtRDR1 and OsRDR1 could commonly inhibit cell-cycle process in all seven cancer cell lines tested but not in any of the non-cancer control cells (Figures 1G, 1H, and S1E; Table S1). More than 30 core cell-cycle genes, including CDCs, CDKs, MCMs (minichromosome maintenance complex components), and ORCs (origin recognition complex subunits), were profoundly suppressed by plant RDR1 in cancer cells (Figure S1F). Notably, short-time (2–3 days) induction

Figure 1. Ectopic expression of plant immune protein RDR1 broadly represses cancer cell proliferation by interfering with cell-cycle process but does not affect non-cancer cells

(A) Schematic representation of ectopic expression of RDR1 proteins in animal cells.
(B and C) Western blot analysis of RDR1 expression in different cell lines.
(D) Images of tagged mCherry-OsRDR1 in living cells. Scale bars, 10 μm.
(E) Growth curves of indicated cell lines with RDR1 expression (n = 3).
(F) Quantification of colonies of indicated cells at day 7 (n = 3).
(G) GSEA pathway analysis in RDR1 expression group. Pathways with p value < 0.05 are considered significant and colored according to the normalized enrichment score (NES).
(H) GSEA enrichment plots. In each plot, left: RDR1(+)Dox group; right: wild-type and RDR1(−)Dox groups.
(I) Western blot analysis of indicated cell-cycle proteins. Asterisk (*) indicates the downregulation of cell-cycle protein expression, compared with control groups.
(J) Quantification of percentages of different cell-cycle phases in indicated cell lines with RDR1 expression (n = 3).
Data are represented as mean ± SD (E, F, and J). n.s., not significant; *p < 0.05, **p < 0.01, ***p < 0.001 by unpaired Student's t test (F and J). FDR was used to correct the p value (E).
See also Figure S1 and Table S1.

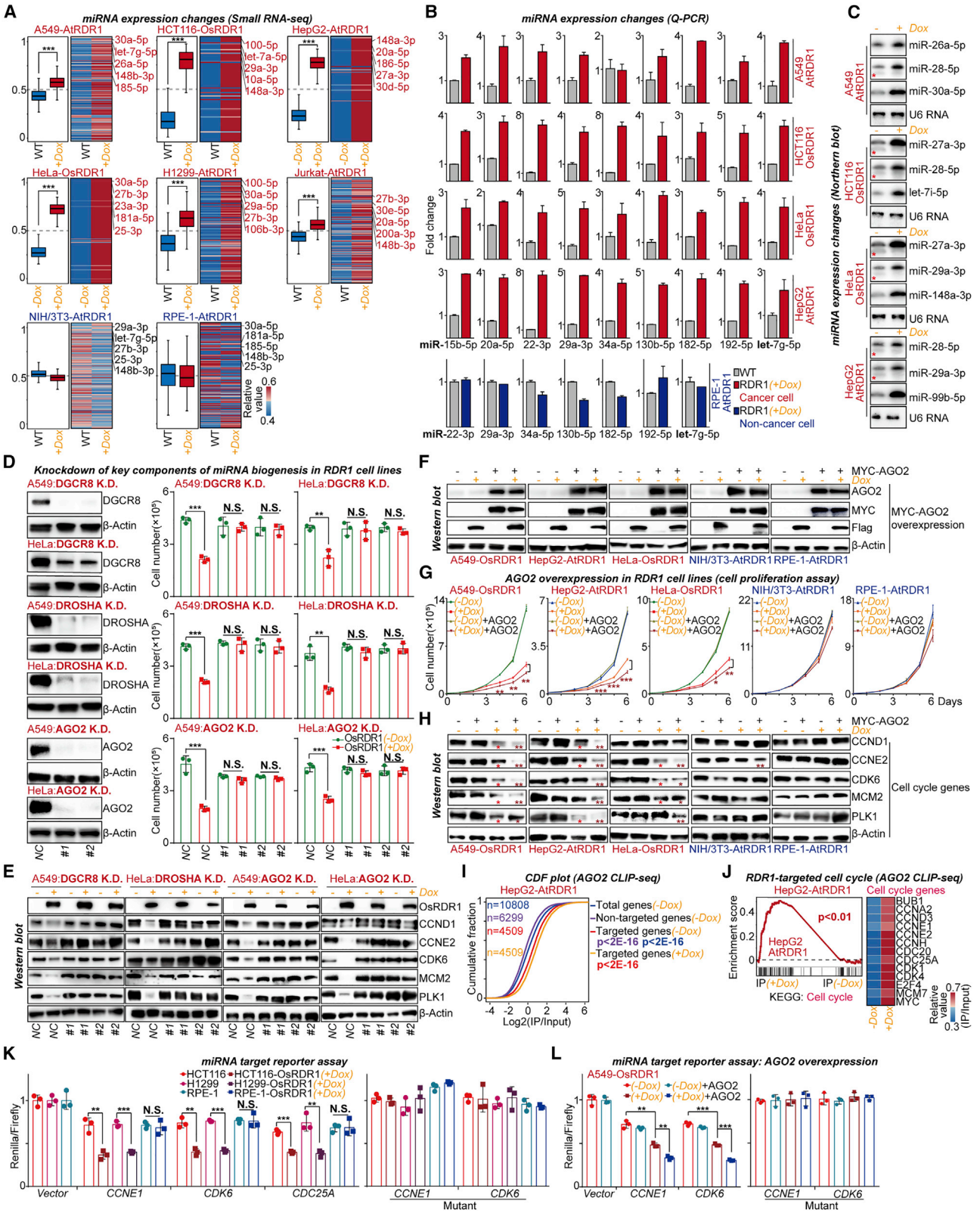

(legend on next page)

of RDR1 can significantly suppress cell-cycle process and related genes in cancer cells (Figures 1E, 1G, 1H, S1E, and S1F–S1H; Table S1), indicating that cell-cycle pathway could be a direct target of RDR1. Western blot further proved that plant RDR1 decreased the expressions of key cell-cycle proteins (including CCND1, CCNE2, CDK6, MCM2, and PLK1) in HeLa, HepG2, H1299, and Jurkat but not in non-cancer RPE-1 and WIBR3 cells (Figure 1I). EdU/PI staining assay revealed that RDR1 expression in HCT116, HepG2, and H1299 cells significantly reduced the cell proportion in the S phase and instead increased cells in the G0/G1 phase. As expected, RDR1 did not affect the cell cycle in non-cancer NIH/3T3 cells (Figure 1J). Thus, we consider plant immune protein RDR1 as an external tumor suppressor, which is able to generally target and interfere with cell-cycle pathway in cancer, but not in non-cancer cells.

Plant RDR1 globally elevates miRNA expression in cancer cells

Since RDR1 participates in small RNA pathways in plants (Borges and Martienssen, 2015; Cao et al., 2014), we hypothesized that RDR1 inhibited cell cycle through small RNAs in animals. Small RNA-seq was performed on cancer and non-cancer control cells with or without RDR1 induction. Genome-wide analysis was firstly performed. However, we did not detect any type of siRNAs originating from dsRNAs at coding gene, transposon, noncoding RNA, or other genomic regions (Table S2), showing that plant RDR1 alone might not be able to reconstitute siRNA pathway in animals. Surprisingly, we did find an obvious increase in global miRNA expression in all cancer, but not in non-cancer, cell lines (Figures 2A and S2A; Table S3). Using both qRT-PCR analysis and small RNA northern blot, we further confirmed the expressional increase of multiple miRNAs in cancer (Figures 2B and 2C). Furthermore, by treating HeLa cells with a cell-cycle inhibitor, palbociclib, we found that cell-cycle arrest cannot cause dramatic accumulation of global miRNA expression, like RDR1 ectopic expression, in cancer cells (Figures S2B and S2C), indicating that miRNA accumulation was not due to cell-cycle arrest. Finally, cumulative distribution function (CDF) plots based on RNA-seq data revealed that miRNA target genes were significantly suppressed by RDR1, compared with non-targeted genes, in cancer cells (Figure S2D). Considering that miRNA deficiency and global miRNA suppression are widely reported and closely related to tumorigenesis in many cancers (Gaur et al., 2007; Lin and Gregory, 2015; Lu et al., 2005), we therefore proposed that plant RDR1 inhibits cell cycle and proliferation by re-elevating global miRNA expression to rescue miRNA deficiency in different cancer cells specifically.

RDR1 uses miRNAs to target cell-cycle genes and inhibit cancer cell proliferation

First, we had to verify whether miRNA pathway was indispensable for the antitumor effects of RDR1. To this end, we knocked down the expression of DROSHA, DGCR8, and AGO2, using synthetic siRNAs, and found that individual depletion of these key components in miRNA pathway all erased the suppressive effects of plant RDR1 on cell-cycle proteins, including CCND1, CCNE2, CDK6, MCM2, and PLK1, as well as cell proliferation (Figures 2D and 2E). Next, we generated cancer and non-cancer control cell lines with consistent AGO2 overexpression (Figures 2F and S2E). We discovered that although AGO2 overexpression alone did not affect cell proliferation, it significantly enhanced the RDR1-mediated inhibition of cancer cell proliferation and cell-cycle proteins in cancer cells (Figures 2G and 2H).

Next, using AGO2 antibody, we performed crosslinking immunoprecipitation (CLIP)-seq analysis in HepG2 cells with or without RDR1 induction (Figure S2F). Using CDF plot analysis, we found that as expected miRNA targets, including cell-cycle genes, were significantly enriched in AGO2 CLIP-seq samples (Figure 2I) compared with the input samples, suggesting a high affinity of miRNA-containing RISCs with target mRNAs. Also, interestingly, RDR1 induction dramatically enhanced the binding and recognition of RISCs with target cell-cycle genes (Figures 2I, 2J, and S2G; Table S1). These results strongly indicated that RDR1 interfered with cell-cycle genes by using a miRNA-mediated regulatory network (Figure S2H).

Figure 2. Plant RDR1 elevates miRNA expression, and miRNA pathway is indispensable for RDR1 antitumor functions

(A) Boxplot and heatmap of expression of miRNAs in each cell line.

(B) qPCR analysis of indicated miRNAs in cells with Dox induction for 6 days. Data were normalized to U2 (HCT116, HeLa) or U6 RNA (A549, HepG2, RPE-1) (n = 2).

(C) Northern blot analysis of indicated miRNAs in cells with Dox induction for 6 days. Asterisk (*) represents 1-nt-shorter miRNA isoforms.

(D) Western blot analysis of indicated proteins after siRNA transfection for 3 days (left panel). Quantification of living cell numbers after siRNA transfection at day 5 (right panel) (n = 3).

(E) Western blot analysis of indicated cell-cycle proteins after siRNA transfection at day 5.

(F) Western blot analysis of the AGO2 and RDR1 expression in indicated cell lines.

(G) Growth curves of the indicated cell lines with RDR1 and AGO2 overexpression (n = 3).

(H) Western blot analysis of indicated cell-cycle proteins. Asterisk (*) indicates the downregulation of cell-cycle protein expression, compared with (−)Dox and AGO2 groups. Double asterisk (**) indicates the downregulation of cell-cycle protein expression, compared with (−)Dox, AGO2, and RDR1 groups.

(I) CDF plot of AGO2 CLIP-seq data. For targeted genes in HepG2-AtRDR1(−)Dox group, the p value in purple is compared with non-targeted genes in HepG2-AtRDR1(−)Dox group, and the p value in blue is compared with total genes in HepG2-AtRDR1(−)Dox group. For targeted genes in HepG2-AtRDR1(+)Dox group, the p value in red is compared with targeted genes in HepG2-AtRDR1(−)Dox group.

(J) Enrichment plots of GSEA and heatmap of representative upregulated cell-cycle genes in AGO2 CLIP-seq data.

(K and L) Renilla to firefly luciferase ratios in indicated cells with RDR1 expression transfected with the *CCNE1*, *CDK6*, and *CDC25A* 3′ UTR-based reporters or mutant versions (n = 3).

Data are presented as mean ± SD (B, D, G, K, and L). n.s., not significant; *p < 0.05, **p < 0.01, ***p < 0.001 by two-sided Wilcoxon rank-sum test (A), unpaired Student's t test (D, G, K, and L), and two-sided Kolmogorov-Smirnov test (I).

See also Figure S2 and Tables S1 and S3.

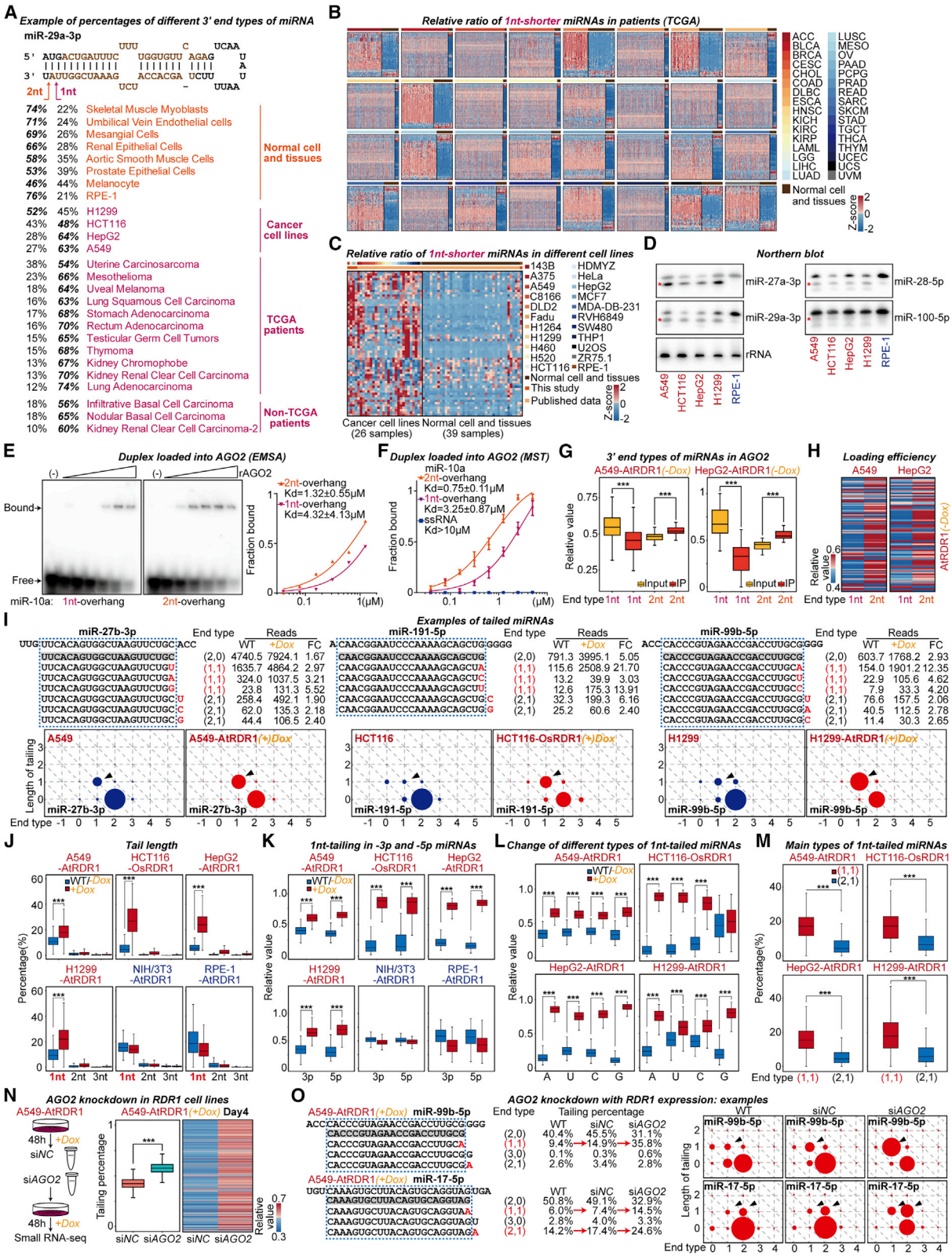

(legend on next page)

To experimentally verify this hypothesis, we cloned 3′ untranslated regions (UTRs), containing miRNA target sites, of cell-cycle genes (including CCNE1, CDK6, and CDC25A) into the dual-luciferase reporter vector, separately, and we used the relative Renilla:firefly luciferase activity to measure the repression efficiency of miRNAs quantitatively (Figure S2I). As expected, RDR1 expression significantly reduced the activity of Renilla luciferase in HCT116 and H1299 cells, with dramatic increase of miRNA dosage, but not in RPE-1 cells (Figures 2A, 2B, and 2K). Furthermore, AGO2 overexpression obviously strengthened the repression of RDR1 on luciferase genes in A549 cells (Figure 2L). By contrast, mutations on miRNA target sites erased all the above repression effects of plant RDR1 on the reporter luciferase in cancer cells with or without AGO2 overexpression (Figures 2K, 2L, and S2I), directly proving that RDR1-mediated targeting and inhibition of cell-cycle genes were through miRNA molecules.

Abnormal miRNA isoforms with 1-nt-shorter 3′ ends are widely accumulated in human primary tumors and cancer cells

We next aimed to understand the mechanism for RDR1-mediated enhancement of miRNA pathway, particularly in cancer cells. We performed large-scale data mining and analysis on published small RNA-seq data, including 9,980 human patient samples belonging to 32 types of cancers from The Cancer Genome Atlas (TCGA) dataset, 62 non-TCGA primary tumor samples belonging to 4 types of cancers, 39 normal healthy tissues, and 26 cancer cell lines from other studies (Table S4). Very surprisingly and interestingly, we found that in many primary tumors and cancer cell lines, 3′ ends of many miRNAs were mainly 1 nt shorter than the annotation, and these 1-nt-shorter miRNAs became the largest population among different miRNA isoforms and much more abundant than normal annotated miRNAs that remained the predominant isoform in healthy control tissues and cells (Figures 3A and S3A; Table S4). These abnormal 1-nt-shorter miRNA isoforms were widely accumulated across all the primary tumor samples, covering around 30%–70% of miRNA populations from uterine carcinosarcoma (UCS) to lung adenocarcinoma (LUAD), as well as in different cancer cell lines (Figures 3B, 3C, and S3B–S3D; Table S4). Experimentally, using small RNA northern blot, we verified the accumulation of 1-nt-shorter isoforms of several quite abundant miRNAs, including miR-27a, -28, and -29a, specifically in cancer A549, HCT116, HepG2, and H1299 cells but not in RPE-1 cells (Figure 3D). Our discovery is consistent with two recently published studies in cutaneous melanoma (Broseghini et al., 2021; Dika et al., 2021).

Notably, we observed that these isoforms with 1-nt-shorter 3′ ends could be detected among both 5p and 3p arms of miRNAs derived from the same precursors (Figures S3A and S3E). Therefore, we proposed that the problematic miRNA duplexes with 1 nt overhang, which are 1 nt shorter than normal miRNA duplexes with 2 nt overhang, could not be loaded into AGO2 protein efficiently to form functional RISCs (Ma et al., 2004), eventually leading to the decrease of global miRNA expression in cancer cells. By *in vitro* incubating recombinant AGO2 (rAGO2) purified from insect cells with synthetic miR-10a duplex isoforms containing 1 or 2 nt overhangs, followed by either gel electrophoresis mobility shift assay (EMSA) or microscale thermophoresis (MST) assay, we indeed proved that 1-nt-overhang miRNA duplexes cannot be loaded into rAGO2 as efficiently as 2-nt-overhang ones (Figures 3E and 3F). Also, *in vivo* in cancer A549 and HepG2 cells, AGO2-immunoprecipitation (AGO2-IP) combined with small RNA-seq revealed that, compared with annotated miRNAs derived from 2-nt-overhang duplexes that were clearly enriched in AGO2-IP sample, 1-nt-shorter miRNAs were much more abundant in input samples than in AGO2-IP samples (Figures 3G and 3H). Thus, in cancer cells abnormal miRNA duplex isoforms with 1 nt overhang cannot be loaded into AGO2 effectively and are unstable (Bartel, 2018; Yu and Kim, 2020), which therefore might be related to the decreased miRNA dosage in different tumors (Gaur et al., 2007; Lu et al., 2005).

Figure 3. Abnormal 1-nt-shorter miRNA isoforms are widely accumulated in different human tumors, and RDR1 modifies these problematic miRNAs by mononucleotide tailing

(A) 3′ end type of selected mature miRNA is shown in stem-loop structures. Percentages are relative to untailed miRNAs. Mature miRNAs with 2 nt overhang are shown in brown.

(B and C) Relative ratio of 1-nt-shorter miRNA isoforms from TCGA patients and cell lines is shown in heatmap. Each row represents one mature miRNA. Full names of 32 cancer types are shown in Table S4.

(D) Northern blot analysis of indicated miRNAs in different cell lines. Asterisk (*) represents accumulation of 1-nt-shorter miRNAs.

(E) Electrophoretic mobility shift assays of the binding of rAGO2 to annealed miR-10a with 1 or 2 nt overhang.

(F) Microscale thermophoresis assays of the binding of rAGO2 to annealed miR-10a with 1 or 2 nt overhang (n = 3).

(G) Different 3′ end type of mature miRNAs in AGO2-IP and small RNA-seq assay.

(H) Loading efficiency of mature miRNAs in AGO2-IP and small RNA-seq assay. Loading efficiency was defined as miRNA expression of IP/input.

(I) miRNA examples with corresponding reads and dot plots displaying the end type. FC, fold change. Tail of each read is shown in red. End type is shown with a number pair: (overhang type, length of tailing). The area of each dot is proportional to percentage of reads of the mature miRNA.

(J) Percentage of the miRNA with a 1–3 nt tail. Total value for calculating the proportion is the sum of miRNA expression in that cell line.

(K) Expression of 1-nt-tailed miRNAs in -3p and -5p miRNAs.

(L) Expression of different types of 1-nt-tailed miRNAs.

(M) Proportion of main end type of 1-nt-tailed miRNAs. Total value for calculating the proportion is the total miRNA expression in the group.

(N) Left panel: schematic representation of AGO2 knockdown in RDR1-stable cell lines. Right panel: boxplot and heatmap showing 1-nt-tailing percentage of AGO2 knockdown group.

(O) Examples of miRNA sequences with different end types and tails are shown in tables and dot plots. Red arrows indicate increases in tailing percentage.

Data are presented as mean ± SEM (F). ***$p < 0.001$ by two-sided Wilcoxon rank-sum test (G and J–N).

See also Figures S3 and S4 and Table S4.

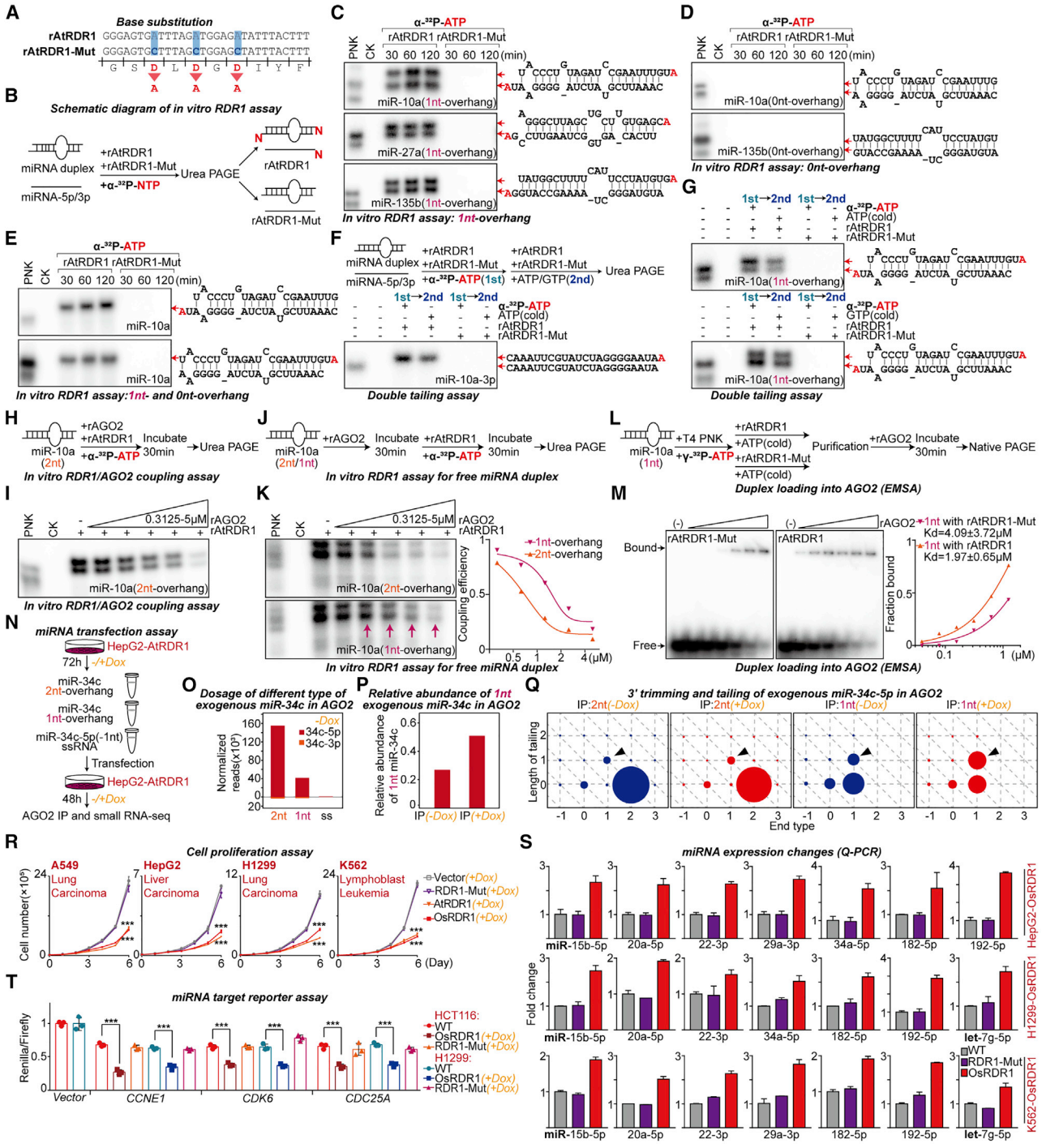

Figure 4. RDR1 can recognize and tail AGO2-dissociated miRNA duplexes with 1 nt overhang to restore their loading efficiency into AGO2 to rescue miRNA deficiency

(A) Constructs used to introduce the catalytic mutations into rAtRDR1. Blue bars indicate substitutions.

(B) Schematic representation of *in vitro* RDR1 assay to verify the tailing ability of RDR1.

(C–E) *In vitro* RDR1 assay using annealed miRNA duplexes with different overhang types. The red arrows represent the tailed miRNA sequences with additional A.

(F) Upper: schematic representation of double tailing assay to verify that RDR1 can only add mononucleotides. Lower: double tailing assay using miR-10a-3p. The red arrows represent the tailed miRNA sequences with additional A.

(G) Double tailing assay using annealed 1-nt-overhang miR-10a. The red arrows represent the tailed miRNA sequences with additional A.

(H) Schematic representation of RDR1 and AGO2 coupling assay.

(legend continued on next page)

RDR1 recognizes and modifies 1-nt-shorter AGO2-free miRNA duplexes by mononucleotide extensions

Very surprisingly, we noticed that mature miRNAs with 3′ end mononucleotide extensions were obviously enriched, corresponding to RDR1 ectopic expression in cancer, but not in non-cancer, cells (Figures 3I and S4A–S4C). RDR1 mainly added mononucleotides, but not two or more nucleotides, to 3′ ends of miRNAs derived from both 5p and 3p arms of miRNA precursors (Figures 3J and 3K). Interestingly, this mononucleotide extension (including A, U, C, or G) mainly appeared on 1-nt-shorter miRNAs but not on miRNAs with annotated cleavage ends (Figures 3L and 3M). Small RNA northern blot further confirmed that RDR1 expression was indeed able to dramatically reduce 1-nt-shorter miRNA isoforms and increase the miRNAs with a correct length in cancer HepG2, HeLa, A549, and HCT116 cells (Figure 2C).

Above all, we propose that plant RDR1 prefers to recognize AGO2-disassociated 1-nt-shorter miRNA (duplex) isoforms—which are accumulated particularly in cancer, but not in non-cancer, cells—as substrates and modifies these problematic miRNAs with mononucleotide tails. To verify this hypothesis *in vivo*, we performed siRNA-mediated AGO2 knockdown in cancer A549 cells with or without RDR1 expression for small RNA-seq analysis (Figures 3N and S4D). As expected, this assay showed that AGO2 depletion can indeed further improve the RDR1-mediated miRNA modification with mononucleotide tailing on both 1-nt-shorter miRNA isoforms and the annotated miRNAs in cancer cells (Figures 3N, 3O, S4E, and S4F). This assay demonstrated that artificial depletion of AGO2 resulted in increased AGO2-disassociated miRNA duplexes, even including annotated miRNAs with 2 nt overhang, which eventually served as suitable substrates for RDR1. Altogether, RDR1 is able to recognize 1-nt-shorter AGO2-disassociated miRNA (duplex) isoforms with 1 nt overhang and modifies these mammalian miRNAs with mononucleotides in cancer cells.

RDR1 can restore the 2 nt overhang structure of problematic miRNA duplexes and their loading efficiency into AGO2

Noting that plant RDR6 has been reported to own both RNA polymerase and nucleotidyltransferase activities (Baeg et al., 2017; Curaba and Chen, 2008), we next set out to characterize the potential nucleotidyltransferase activity of RDR1 protein on mammalian miRNAs. AtRDR1 was cloned into pETDuet-1 vector for expression in bacteria, and three-amino-acids mutation (Asp-to-Ala, *3DA*) at the key catalytic site that was conserved in different species was further generated to produce a mutant version of recombinant AtRDR1 (rAtRDR1), losing enzymatic activity (Figures 4A, S5A, and S5B). After *in vitro* expression and purification, wild-type (WT) and *3DA* mutant rAtRDR1 were incubated with α-^{32}P-labeled NTPs and different synthetic miRNA isoforms for miRNA tailing assay (Figure 4B). This assay firstly showed that WT rAtRDR1 can add mononucleotides to 3′ end of single-stranded mature miRNAs with different lengths, whereas *3DA* mutation destroyed this nucleotidyltransferase activities of RDR1 (Figures S5C and S5D). Interestingly, we found that WT, but not *3DA* mutant, rAtRDR1 was able to mediate the mononucleotide modification of miRNA duplexes with 1 or 2 nt overhangs, but not the ones with blunt ends (Figures 4C–4E and S5E). Furthermore, we performed RDR1 double tailing assay by using α-^{32}P-labeled ATP, followed by non-radioactive ATP/GTP, and this assay clearly showed that RDR1 can only add mononucleotides once to miRNA substrates (Figures 4F and 4G), which is consistent with the biochemical features of other nucleotidyltransferase enzymes such as TUTase and fungus RDR (Aalto et al., 2010; D'Ambrogio et al., 2012; Heo et al., 2012; Katoh et al., 2009; Yu and Kim, 2020).

To prove our hypothesis that RDR1 prefers to recognize AGO2-free miRNA duplex isoforms with 1 nt overhang as substrates, rather than normal 2-nt-overhang miRNA duplexes, we performed *in vitro* RDR1/AGO2 coupling assays. Firstly, we co-incubated 2-nt-overhang miRNA duplexes with both rAGO2 and rAtRDR1 proteins (Figure 4H), as well as α-^{32}P-labeled ATP, which clearly revealed that AGO2 protein can interfere with the RDR1-mediated miRNA tailing reactions dosage dependently (Figure 4I), suggesting a direct competition between AGO2 and RDR1 proteins on the recognizing and binding of miRNA duplexes, which is consistent with the previous result showing that AGO2 depletion could greatly enhance RDR1-mediated miRNA tailing events in cancer cells *in vivo* (Figures 3N, 3O, and S4D–S4F). Furthermore, we pre-incubated rAGO2 with miRNA duplexes with 1 nt/2 nt overhangs for 30 min

(I) RDR1 and AGO2 coupling assay using annealed miR-10a with 2 nt overhang.
(J) Schematic representation of *in vitro* RDR1 assay for free miRNA duplex.
(K) *In vitro* RDR1 assay using annealed miR-10a with 1 or 2 nt overhang. Annealed miR-10a incubated with rAtRDR1 only was used as a negative control.
(L) Schematic representation of electrophoretic mobility shift assays to verify that rAtRDR1 can modify 1-nt-shorter miRNA duplexes to increase their loading efficiency.
(M) Electrophoretic mobility shift assays of the binding of rAGO2 to 1-nt-overhang miR-10a incubated with rAtRDR1 or rAtRDR1-Mut. The probe incubated with rAtRDR1 or rAtRDR1-Mut only was used as a negative control.
(N) Schematic representation of miR-34c transfection assay in HepG2-AtRDR1 stable cell lines.
(O) Normalized reads of exogenous miR-34c in AGO2-IP are shown in bar plot.
(P) Relative abundance of 1 nt exogenous miR-34c in AGO2 shown in bar plot.
(Q) Examples of miRNA isoforms of exogenous miR-34c-5p are shown in dot plots.
(R) Growth curves of indicated cells with RDR1-Mut or wild-type OsRDR1 expression (n = 3).
(S) qRT-PCR analysis of indicated miRNAs in cells with Dox induction for 6 days. Data were normalized to U2 (H1299 and K562) or U6 RNA (HepG2) (n = 2).
(T) Renilla to firefly luciferase ratios in cells with OsRDR1 or RDR1-Mut expression transfected with the *CCNE1*, *CDK6*, and *CDC25A* 3′ UTR-based reporters (n = 3).
Data are presented as mean ± SD (R–T). ***$p < 0.001$ by unpaired Student's t test (R and T).
See also Figure S5.

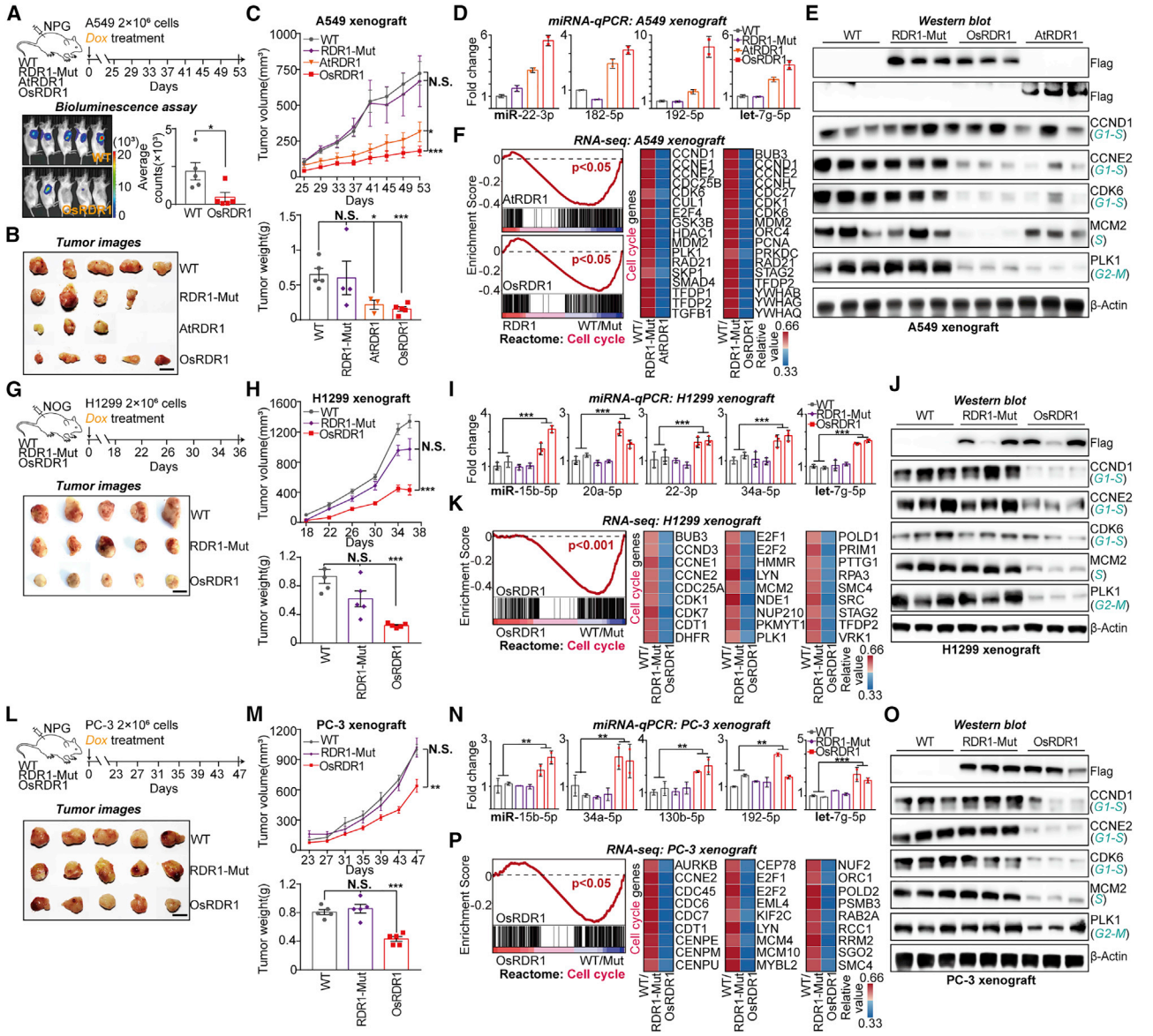

Figure 5. RDR1 suppresses solid tumor growth in mice *in vivo*

(A) Top: schematic representation of the A549 xenograft model. Bottom: representative bioluminescent images of mice at day 52 (left panel) and quantification of tumor luciferase counts (right panel).

(B) Images of tumors dissected from (A) at day 53 post-transplantation. Scale bars, 1 cm.

(C) Growth curves and the weight of tumors in (A).

(D) qRT-PCR analysis for tumors dissected from mice in (A) (n = 2).

(E) Western blot analysis of lysates from tumors dissected from (A) (n = 3).

(F) Enrichment plots of GSEA and heatmap of representative downregulated cell-cycle genes in A549 xenograft RNA-seq data.

(G) Top: schematic representation of the H1299 xenograft model. Bottom: images of tumors dissected at day 36 post-transplantation. Scale bars, 1 cm.

(H) Growth curves and the weight of tumors in (G).

(I) qRT-PCR analysis for tumors dissected from mice in (G) (n = 2).

(J) Western blot analysis of lysates from tumors dissected from (G) (n = 3).

(K) Enrichment plots of GSEA and heatmap of representative downregulated cell-cycle genes in H1299 xenograft RNA-seq data.

(L) Top: schematic representation of the PC-3 xenograft model. Bottom: images of tumors dissected at day 47 post-transplantation. Scale bars, 1 cm.

(M) Growth curves and the weight of tumors in (L).

(N) qRT-PCR analysis for tumors dissected from mice in (L) (n = 2). Data were normalized to U2 RNA.

(legend continued on next page)

and then added rAtRDR1 and α-^{32}P-labeled ATP for miRNA tailing assay (Figure 4J). This analysis revealed that since 2-nt-overhang miRNA duplexes can be loaded into AGO2 efficiently (Figures 3E–3H), they were occupied predominantly by increased rAGO2 and therefore could not be further recognized and modified by RDR1. Comparably, 1-nt-overhang miRNA duplexes with low AGO2 affinity could be modified by RDR1 after pre-incubation with similar concentrations of rAGO2 proteins as for 2-nt-overhang duplexes (Figure 4K).

At last, we performed *in vitro* RDR1 tailing assay using 1-nt-shorter miRNA duplexes with 1 nt overhang, and the products of which were then purified for miRNA/AGO2 loading assay (Figure 4L). We found that, compared with *3DA* mutant rAtRDR1 that cannot mediate miRNA modification, by mononucleotide tailing, WT rAtRDR1 was able to modify 1-nt-shorter miRNA duplexes and repair their 2 nt overhang to greatly increase their loading efficiency into rAGO2 (Figure 4M). Furthermore, *in vivo*, we performed AGO2-IP followed by small RNA-seq analysis in A549 and HepG2 cells expressing AtRDR1. miRNA isoforms with mononucleotide tails, which might be mainly modified by RDR1, can be successfully and efficiently loaded into AGO2 protein, similarly to normal untailed miRNAs derived from duplexes with 2 nt overhang (Figures S5F–S5H). Finally, we transfected the same number of miR-34c duplexes with 1 or 2 nt overhangs and single-stranded miR-34c-5p, separately, into cancer HepG2 cells with RDR1 expression, in which expression of miR-34c cannot be detected; here, AGO2-IP followed by small RNA-seq analysis demonstrated that, compared with 2-nt-overhang miR-34c duplexes that can be efficiently loaded into AGO2, 1-nt-overhang miR-34c duplexes loaded into AGO2 were significantly reduced, whereas single-stranded miR-34c-5p could not be detected in AGO2-IP samples (Figures 4N, 4O, and S5I). Notably, only 5p strand of miR-34c duplexes was retained in AGO2-IP samples, and miR-34c-3p was mainly degraded (Figure 4O), confirming the previously known strand selection process during AGO/miRNA complex formation (Bartel, 2018). Further detailed analysis on miRNA isoforms revealed that for 2-nt-overhang miR-34c duplexes around 70% of miRNAs loaded into AGO2 were original sequences without tailing modification, which were not affected by ectopic RDR1 expression. However, comparably, for 1-nt-overhang miR-34c duplexes, only no more than 40% of AGO2-binding miRNAs were derived from original duplexes, and miRNAs with mononucleotide modifications, which were clearly strengthened by RDR1 expression, became a main population (Figures 4P, 4Q, S5J, and S5K).

Altogether, we concluded that RDR1 owning nucleotidyltransferase activity is able to recognize and modify AGO2-disassociated 1-nt-shorter miRNA duplex isoforms with 1 nt overhang with mononucleotide tails to restore their AGO2 loading efficiency and eventually repair the defective miRNA pathway in cancers.

The nucleotidyltransferase activity is indispensable for RDR1 to elevate miRNA expression, target cell-cycle genes, and inhibit cancer cell proliferation

To prove the above conclusion in cancer cells *in vivo*, we generated different cancer cell lines expressing *3DA* mutant OsRDR1 protein. We found that after Dox induction, although WT and *3DA* mutant OsRDR1 proteins were expressed at a similar level, mutant RDR1 lost the ability to inhibit tumor cell (containing A549, HepG2, H1299, and K562) proliferation (Figures 4R and S5L). Different from WT protein, *3DA* mutant RDR1 cannot elevate miRNA expression in cancer cells (Figure 4S). Finally, miRNA target gene reporter assay showed that *3DA* mutant RDR1 was not able to repress expression of cell-cycle genes, including CCNE1, CDK6, and CDC25A, in HCT116 and H1299 cancer cells (Figure 4T). In addition, transcriptomic analysis showed that mutant RDR1 lost the suppressive impacts on cell-cycle pathways and genes in H1299 and K562 cells *in vivo* (Figure S5M).

RDR1 suppresses solid tumor growth in mice *in vivo*

We next thought to measure the antitumor effects of plant RDR1 in mice *in vivo*. Firstly, we performed mouse xenograft analysis by injecting RDR1-inducible cancer cells into immunodeficient mice for tumor formation; ectopic expression of RDR1 can be realized by feeding mice with water containing Dox. A549 cells with consistent luciferase gene expression were used for *in vivo* imaging of tumorigenesis in mice. Bioluminescence assay showed that, after around 7 weeks, the signaling density of tumor tissues was greatly reduced in mice injected with A549 cells with OsRDR1 induction (Figure 5A). We found that WT RDR1 can significantly reduce the tumor size, volume, and weight, but *3DA* mutant RDR1 protein cannot (Figures 5B and 5C). qRT-PCR and western blot analyses indicated that WT, but not *3DA* mutant, RDR1 dramatically increased the expression of miRNAs, including miR-22, -182, -192, and let-7g, and reduced several key cell-cycle proteins containing CCND1, CCNE2, CDK6, PLK1, and MCM2 in xenograft tumor tissues (Figures 5D and 5E). Finally, global transcriptomic analysis showed that plant RDR1 was able to significantly suppress cell-cycle pathway by inhibiting many cell-cycle genes in A549-derived xenograft tumors in NPG (NOD.Cg-*Prkdc*^{scid}*Il2rg*^{tm1Vst}/Vst) mice (Figure 5F).

Similarly, we injected H1299 and PC-3 cells with inducible WT or *3DA* mutant RDR1 expression into NOG (NOD.Cg-*Prkdc*^{scid}*Il2rg*^{tm1Sug}/JicCrl) or NPG mice for xenograft analysis. Here, we detected that WT, but not mutant, RDR1 greatly inhibited tumor size, volume, and weight. We also found that plant RDR1 was able to dramatically elevate miRNA expression to further inhibit cell-cycle process in cancer cells in xenografts derived from H1299 or PC-3 cells *in vivo* (Figures 5G–5P and S6A–S6C; Table S5).

(O) Western blot analysis of lysates from tumors dissected from (L) (n = 3).

(P) Enrichment plots of GSEA and heatmap of representative downregulated cell-cycle genes in PC-3 xenograft RNA-seq data.

Data are presented as mean ± SD (D, I, and N) or mean ± SEM (A, C, H, and M). n.s., not significant; *p < 0.05, **p < 0.01, ***p < 0.001 by unpaired Student's t test (A, C, H, I, M, and N).

See also Figure S6 and Table S5.

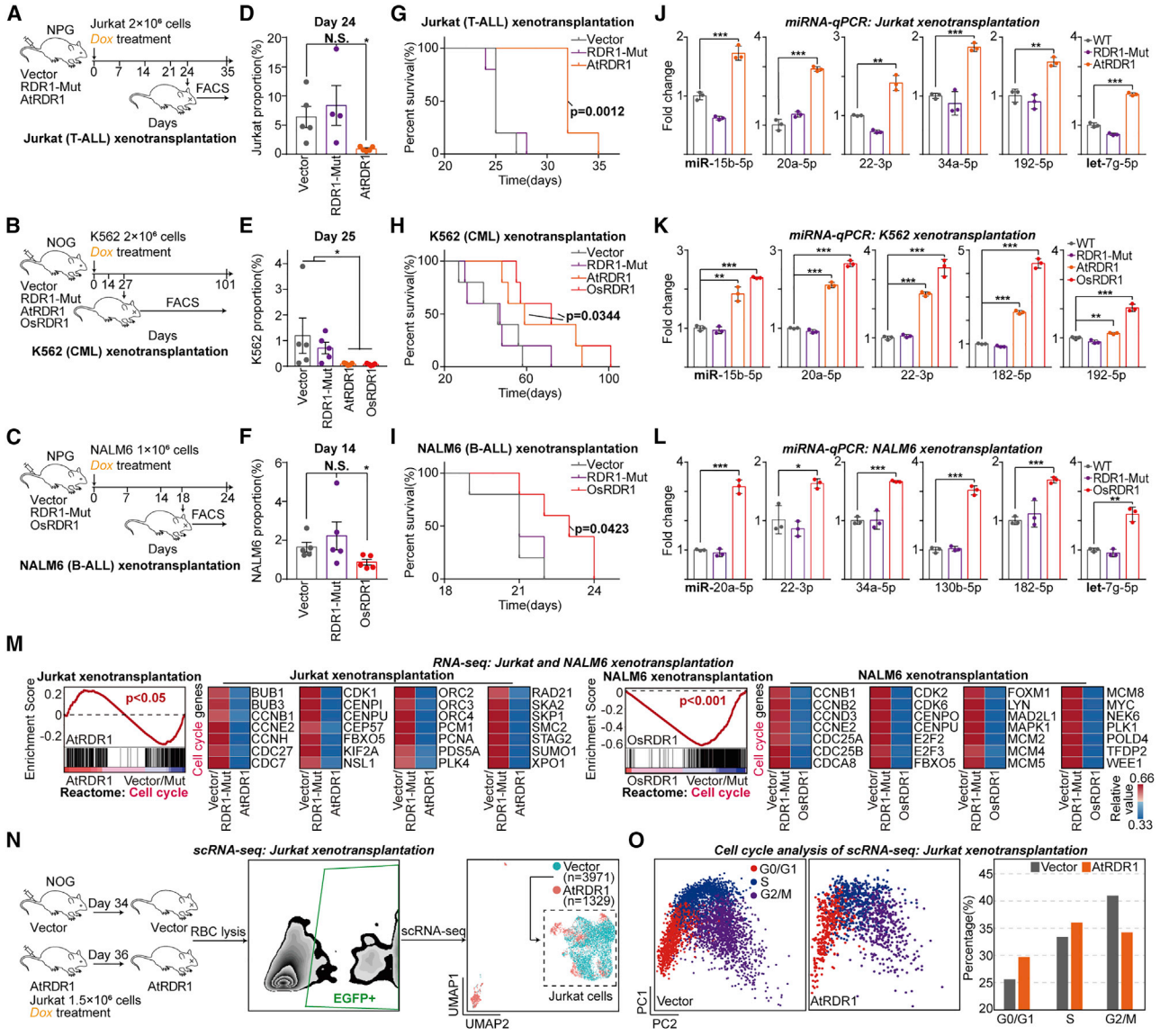

Figure 6. RDR1 inhibits leukemia proliferation in mice *in vivo*

(A–C) Schematic representation of the xenotransplantation model in NPG (A and C) or NOG (B) immunodeficient mice injected with Jurkat (A), K562 (B), and NALM6 (C) cell lines.

(D–F) Quantification of the proportion of Jurkat (D), K562 (E), and NALM6 (F) cells in the peripheral blood of mice in (A)–(C) (n = 5).

(G–I) Survival curves for mice in (A)–(C).

(J–L) qRT-PCR analysis of indicated miRNAs in sorted EGFP+ cells from (A) to (C).

(M) Enrichment plots of GSEA and heatmap of representative downregulated cell-cycle genes in Jurkat and NALM6 xenotransplantation RNA-seq data.

(N) Schematic representation of scRNA-seq of Jurkat xenotransplantation model.

(O) Cell-cycle phases of cells in scRNA-seq data shown in scatter diagram and bar chart.

Data are presented as mean ± SD (J–L) or mean ± SEM (D–F). n.s., not significant; *p < 0.05, **p < 0.01, ***p < 0.001 by unpaired Student's t test (D–F and J–L) and log-rank test (G–I).

See also Figure S6 and Tables S5 and S6.

RDR1 inhibits leukemia proliferation in mice *in vivo*

We next evaluated the antitumor effects of RDR1 in leukemia mouse models *in vivo*. We injected three leukemia cell lines, including Jurkat, K562, and NALM6, with inducible WT or *3DA* mutant RDR1 expression into NPG or NOG mice, respectively (Figures 6A–6C). Compared with vector control or mutant RDR1, WT RDR1 was able to significantly inhibit cell proliferation of all three leukemia cell lines (Jurkat, K562, and NALM6) (Figures 6D–6F; Table S6) and eventually extended the lifespan of xenotransplantation mice (Figures 6G–6I). WT, but not *3DA* mutant, RDR1 can increase miRNA expression dramatically in leukemia cells in mice *in vivo*

(Figures 6J–6L). Additionally, we performed polyA(+) RNA-seq for transcriptomic comparison, which showed that plant RDR1 enabled inhibition of cell-cycle pathway by repressing key cell-cycle factors, including CDK1, CCNE2, PLK1, and CDK6, in both Jurkat and NALM6 leukemia cells in animal models (Figures 6M, S6D, and S6E; Table S5). To precisely measure the suppressive effect of RDR1 on cell-cycle process in leukemia cells, we isolated donor Jurkat cells from xeno-transplantation mice for single-cell (sc) RNA-seq analysis (Figures 6N, S6F, and S6G), which showed that RDR1 retained Jurkat cells in G0/G1 stage in mice, supporting that RDR1 inhibited cell proliferation by repressing cell-cycle process in leukemia cells (Figures 6O and S6H).

RDR1-containing nanoparticles can be used to inhibit cancer cell proliferation

Next, we tested the possibility of RDR1 delivery *in vitro* and *in vivo* by using different stratagems. WT and *3DA* mutant rAtRDR1 proteins expressed and purified *in vitro* were mixed with red fluorescent R-phycoerythrin (R-PE) protein, separately, to generate nanoparticles, which were then applied for transfection into both cancer and non-cancer cells. After 24 h, R-PE-positive cells with successful transfection were isolated using FACS and cultured for further analysis (Figure 7A). Compared with R-PE control and *3DA* mutant rAtRDR1 proteins, WT rAtRDR1 significantly inhibited proliferation of cancer cells, including A549, HeLa, and H1299, whereas it did not affect non-cancer cells NIH/3T3 and RPE-1 (Figure 7B). Using qRT-PCR analysis, we revealed that WT, but not *3DA* mutant, rAtRDR1 protein delivered by nanoparticles dramatically increased the accumulation of miRNAs particularly in cancer cells but not in non-cancer RPE-1 cells (Figure 7C). Further transcriptomic comparison indicated that nanoparticle-delivered rAtRDR1 protein inhibited cell-cycle pathway significantly by targeting many cell-cycle genes, including CCNE1, CDK1, MCM4, and PLK4, in cancer cells (Figures 7D, S7A, and S7B; Table S5).

RDR1 delivered by AAV inhibit solid tumor growth in mice *in vivo*

Finally, we tested the possibility of RDR1 delivery *in vivo* in mice by using AAV-delivery system (Wang et al., 2019). We cloned OsRDR1 gene into an AAV vector, and after *in vitro* purification, viral particles expressing OsRDR1 and control EGFP were injected separately into 26-day-old xenograft tumors (around 100 mm^3) that were derived from A549 cells in NPG mice, and 50 days later the xenograft tumors were isolated for detailed characterization (Figure 7E). RDR1 delivered by AAV significantly reduced tumor size and weight (Figures 7E and 7F). qRT-PCR and western blot analysis suggested that AAV-delivered OsRDR1 was able to dramatically increase miRNA expression to further target and silence cell-cycle genes such as CDK6, CCNE2, PLK1, and MCM2 in tumor tissues *in vivo* (Figures 7G and 7H). Transcriptomic comparison proved that OsRDR1 inhibited cell-cycle pathway in the AAV-delivery xenograft mice model (Figures 7I, S7C, and S7D; Table S5). In summary, AAV-delivery system can be used to deliver RDR1 to suppress solid tumor growth *in vivo*.

DISCUSSION

miRNAs have been identified and studied for around 30 years (Lee et al., 1993; Wightman et al., 1993). An increasing number of miRNAs have been reported as tumor suppressors or as oncogenic miRNAs. Clinical trials have been initiated by using either miRNA mimics to rescue miRNA functions as tumor suppressors or by using synthetic antisense oligonucleotides to block oncogenic miRNAs. However, these tests all face many challenges at the preliminary clinical phase due to strong toxicological effects (Rupaimoole and Slack, 2017; Slack and Chinnaiyan, 2019).

Interestingly, previous studies indicated that reduction of miRNA expression and deficient miRNA pathway are very important for tumorigenesis (Lin and Gregory, 2015; Lu et al., 2005; Ramírez-Moya et al., 2019; Walz et al., 2015). However, the distinct features of miRNA isoforms have not been systematically described in cancer. By large-scale data mining of published small RNA-seq data covering more than 10,000 human primary patient samples, we discovered abnormal accumulation of 1-nt-shorter miRNA isoforms, widely and particularly existing in many different human primary tumors and cancer cell lines but not in healthy tissues or non-cancer cell lines. We propose that the generation of unusual miRNA duplexes with 1 nt overhang, which cannot efficiently be loaded into AGO2 to form functional RISCs, might be a potential cause for the accumulation of 1-nt-shorter miRNA isoforms in cancer cells. However, after analyzing the published RNA-seq data about the mutants and expressional level of known components participating in miRNA biogenesis or metabolism, we have not found any potential common pathogenic drivers taking part in the abnormal and widespread accumulation of shorter miRNA isoforms in different human cancers, suggesting an unknown mechanism that needs to be further explored in the future.

Nevertheless, our data revealed that plant immune protein RDR1 owning nucleotidyltransferase activity is able to recognize 1-nt-shorter miRNA duplexes that are poorly associated with AGO2 as substrates and to modify these miRNAs by adding mononucleotide tails. This function of RDR1 restores the 2 nt overhang of miRNA duplexes to allow the enhancement of miRNA/AGO2 association and stabilization of miRNAs and therefore can increase miRNA dosage to eventually reactivate deficient miRNA pathway particularly in cancer, but not in non-cancer, cells. Thus, compared with previous strategies of targeting particular oncogenic or tumor-suppressive miRNA(s), RDR1-mediated reactivation and enhancement of defective miRNA pathway, particularly in cancer cells, might be an effective and broad antitumor stratagem with limited toxicological effects on healthy tissues.

Multiple clinical trials studying the application of cell-cycle inhibitors in cancer therapies are ongoing, and a few of them have been successfully used in clinics (Malumbres and Barbacid, 2009; Otto and Sicinski, 2017; Suski et al., 2021). However, similarly to many other pharmacological compounds for targeted therapy, cell-cycle inhibitors cannot overcome drug resistance caused by cell-cycle gene redundancy and tumor cell heterogeneity (Holohan et al., 2013). Interestingly, essential cell-cycle genes are targeted and post-transcriptionally suppressed by many different miRNAs. Although previous studies focusing on particular oncogenic or tumor-suppressive miRNAs have shown

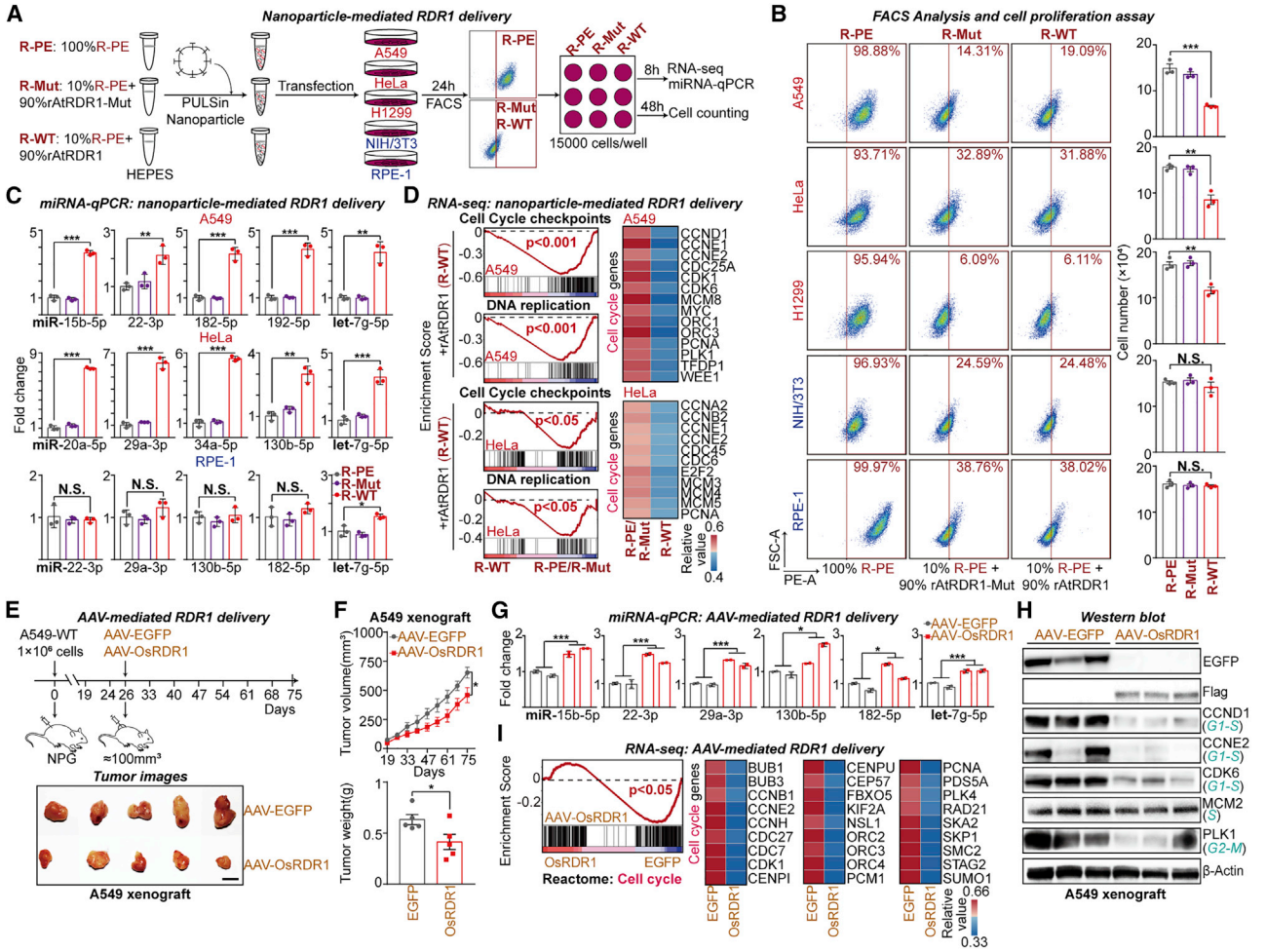

Figure 7. RDR1 delivered by nanoparticles and AAV can inhibit cancer cell proliferation *in vitro* and solid tumor growth in mice *in vivo*, respectively

(A) Schematic representation of nanoparticle-mediated RDR1 delivery. R-PE, 100% R-phycoerythrin (R-PE) control proteins. R-Mut, 10% R-PE proteins and 90% rAtRDR1-Mut proteins. R-WT, 10% R-PE proteins and 90% rAtRDR1 proteins.

(B) Flow cytometry analysis of R-PE+ cells (left panel) and quantification of living cell numbers after delivery (right panel) (n = 3).

(C) qRT-PCR analysis of indicated miRNAs in cells after delivery.

(D) Enrichment plots of GSEA and heatmap of representative downregulated cell-cycle genes in RNA-seq data of A549 and HeLa cells after nanoparticle-mediated RDR1 delivery.

(E) Top: schematic representation of AAV-mediated RDR1 delivery in A549 xenograft model. Bottom: images of tumors dissected from mice at day 75 post-transplantation. Scale bars, 1 cm.

(F) Growth curves and the weight of tumors in (E).

(G) qRT-PCR analysis of indicated miRNAs in tumors in (E).

(H) Western blot analysis of lysates from tumors dissected from (E) (n = 3).

(I) Enrichment plots of GSEA and heatmap of representative downregulated cell-cycle genes in RNA-seq data of AAV-mediated RDR1 delivery in A549 xenograft.

Data are presented as mean ± SD (B, C, and G) or mean ± SEM (F). n.s., not significant; *p < 0.05, **p < 0.01, ***p < 0.001 by unpaired Student's t test (B, C, F, and G).

See also Figure S7 and Table S5.

that these miRNAs can individually participate in tumorigenesis, it seems to be that all biological processes are controlled by multiple different miRNAs. We therefore suggest that miRNAs mediate a network regulation to eventually govern different biological processes as "cellular buffer," and global miRNA dosage plays critical roles in cell fate transitions (Cui et al., 2021; DeVeale et al., 2021; Du et al., 2018; Lin and Gregory, 2015). We revealed that plant RDR1 is able to reactivate defective miRNA pathway, leading to an increase of global miRNA dosage in cancer cells. Therefore, RDR1 efficiently and broadly enables miRNA-mediated network inhibition of the cell-cycle process, which is different from all previous stratagems.

There are various small RNA pathways in different species. RDR, which is lacking in mammals with secondary immunity, is

the key component for siRNA pathways in plants. Here, although we have successfully expressed plant RDR1 proteins in mammalian cells, these cross-species bioengineered RDR1 proteins fail to rebuild an artificial siRNA pathway. One explanation is that other cofactors of RDR are required to synthesize dsRNAs or that mammalian cells own certain control system(s) to prevent the production of siRNAs or dsRNAs. Surprisingly and unpredictably, we found that RDR1 protein with RNA nucleotidyltransferase activity can modify mammalian miRNAs to eventually restore and partake in miRNA pathway in cancer cells, although none of the RDR proteins has been reported to be involved in miRNA pathway in plants or other species. It is very interesting that several known nucleotidyltransferases, including TUTs and RDRs, all add mononucleotide tails to RNA substrates; however, a detailed biochemical explanation is still required.

Limitations of the study

In this study, we discovered that abnormal 1-nt-shorter miRNA isoforms are widely and generally accumulated in many different human primary tumors and cancer cell lines, but not in healthy tissues and non-cancer cell lines, whereas the underlying mechanism still needs to be explored. RDR protein can be further optimized based on evolutionary conservation to obtain the minimal peptide for the future drug development, and many different delivery systems should be tested to eventually realize targeting different types of tumors.

STAR★METHODS

Detailed methods are provided in the online version of this paper and include the following:

- KEY RESOURCES TABLE
- RESOURCE AVAILABILITY
  - Lead contact
  - Materials availability
  - Data and code availability
- EXPERIMENTAL MODEL AND SUBJECT DETAILS
  - Mice
  - Cell culture
- METHOD DETAILS
  - Generation of stable cell lines
  - Western blot
  - RDR1 localization
  - Cell proliferation assay
  - Colony formation
  - Wound healing assay and cell invasion assay
  - EdU/PI staining
  - Total RNA extraction and q.RT-PCR
  - Northern blot
  - Luciferase reporter assay
  - siRNA knockdown
  - Electrophoretic mobility shift assay
  - Microscale thermophoresis assay
  - Recombinant proteins expression and purification
  - *In vitro* RNA-dependent RNA polymerase assay
  - *In vitro* RNA-dependent RNA polymerase and AGO2 assay
  - Adeno-associated virus (AAV) production
  - *In vivo* tumor models
  - *In vitro* nanoparticle-mediated RDR1 delivery
  - RNA-seq
  - Small RNA-seq
  - AGO2 CLIP-seq
  - miRNA transfection assay
  - Single-cell RNA sequencing
  - PolyA(+) RNA-seq analysis
  - Gene set enrichment analysis
  - Prediction of miRNA targets and CDF plots of target genes
  - Processing of small RNA-seq data and annotation of small RNAs
  - Alignment of miRNAs
  - Annotation for sequences aligned to miRNA reference
  - Normalization of miRNA data
  - Tailing analysis and end type analysis of small RNA-seq data
  - Analysis of miRNA isoform for TCGA patient samples and published data
  - Single-cell RNA-seq data analysis
- QUANTIFICATION AND STATISTICAL ANALYSIS

SUPPLEMENTAL INFORMATION

Supplemental information can be found online at https://doi.org/10.1016/j.cell.2022.04.030.

ACKNOWLEDGMENTS

We thank Dr. Cheng Li (Peking University) for helpful discussions about the manuscript; Dr. Xiaowei Chen (Peking University) for kindly providing the AAV plasmids and helping to purify viral particles; Drs. Jiazhi Hu and Hsiang-Ying Lee (Peking University) for kindly providing the human U-2 OS and K562 cell lines, respectively; and Shitang Huang from the Isotope Laboratory for his kind help with and advice on our *in vitro* biochemical experiments. We also thank the flow cytometry Core at the National Center for Protein Sciences at Peking University, particularly Hongxia Lyu and Huan Yang, for technical help and the Core Facilities of Life Sciences, Peking University, for assistance in confocal microscopy and 10X Genomics SC Chromium. We really appreciate the support from Beijing Vitalstar Biotechnology Co., Ltd and Beijing Vital River Laboratory in mouse xenograft model. Graphical abstract was created with BioRender. This work was supported by a grant to P.D. from the Natural Science Foundation of China (32050214 and 32090012) and Qidong-SLS Innovation Fund.

AUTHOR CONTRIBUTIONS

Y.Q. performed most experiments with some help from S.Z. and S.Y. L.D. performed all the bioinformatics analyses with some help from Y.Q. P.D., Y.Q., and H.W. designed all experiments and analyzed data. P.D., Y.Q., and J.O. wrote the manuscript with input from and Y.L. and H.W.

DECLARATION OF INTERESTS

Patents related to the data presented have been filed. The authors declare no competing interests.

Received: August 9, 2021
Revised: February 18, 2022
Accepted: April 26, 2022
Published: May 26, 2022

REFERENCES

Aalto, A.P., Poranen, M.M., Grimes, J.M., Stuart, D.I., and Bamford, D.H. (2010). In vitro activities of the multifunctional RNA silencing polymerase QDE-1 of Neurospora crassa. J. Biol. Chem. *285*, 29367–29374. https://doi.org/10.1074/jbc.M110.139121.

Baeg, K., Iwakawa, H.O., and Tomari, Y. (2017). The poly(A) tail blocks RDR6 from converting self mRNAs into substrates for gene silencing. Nat. Plants *3*, 17036. https://doi.org/10.1038/nplants.2017.36.

Bartel, D.P. (2018). Metazoan microRNAs. Cell *173*, 20–51. https://doi.org/10.1016/j.cell.2018.03.006.

Bernstein, E., Caudy, A.A., Hammond, S.M., and Hannon, G.J. (2001). Role for a bidentate ribonuclease in the initiation step of RNA interference. Nature *409*, 363–366. https://doi.org/10.1038/35053110.

Bolger, A.M., Lohse, M., and Usadel, B. (2014). Trimmomatic: a flexible trimmer for Illumina sequence data. Bioinformatics *30*, 2114–2120. https://doi.org/10.1093/bioinformatics/btu170.

Borges, F., and Martienssen, R.A. (2015). The expanding world of small RNAs in plants. Nat. Rev. Mol. Cell Biol. *16*, 727–741. https://doi.org/10.1038/nrm4085.

Broseghini, E., Dika, E., Londin, E., and Ferracin, M. (2021). MicroRNA isoforms contribution to melanoma pathogenesis. Noncoding RNA *7*, 63. https://doi.org/10.3390/ncrna7040063.

Bueno, M.J., and Malumbres, M. (2011). MicroRNAs and the cell cycle. Biochim. Biophys. Acta *1812*, 592–601. https://doi.org/10.1016/j.bbadis.2011.02.002.

Cao, M., Du, P., Wang, X., Yu, Y.Q., Qiu, Y.H., Li, W., Gal-On, A., Zhou, C., Li, Y., and Ding, S.W. (2014). Virus infection triggers widespread silencing of host genes by a distinct class of endogenous siRNAs in Arabidopsis. Proc. Natl. Acad. Sci. USA *111*, 14613–14618. https://doi.org/10.1073/pnas.1407131111.

Cong, L., Ran, F.A., Cox, D., Lin, S., Barretto, R., Habib, N., Hsu, P.D., Wu, X., Jiang, W., Marraffini, L.A., and Zhang, F. (2013). Multiplex genome engineering using CRISPR/Cas systems. Science *339*, 819–823. https://doi.org/10.1126/science.1231143.

Cui, Y., Lyu, X., Ding, L., Ke, L., Yang, D., Pirouz, M., Qi, Y., Ong, J., Gao, G., Du, P., and Gregory, R.I. (2021). Global miRNA dosage control of embryonic germ layer specification. Nature *593*, 602–606. https://doi.org/10.1038/s41586-021-03524-0.

Curaba, J., and Chen, X. (2008). Biochemical activities of Arabidopsis RNA-dependent RNA polymerase 6. J. Biol. Chem. *283*, 3059–3066. https://doi.org/10.1074/jbc.M708983200.

D'Ambrogio, A., Gu, W., Udagawa, T., Mello, C.C., and Richter, J.D. (2012). Specific miRNA stabilization by Gld2-catalyzed monoadenylation. Cell Rep. *2*, 1537–1545. https://doi.org/10.1016/j.celrep.2012.10.023.

Denli, A.M., Tops, B.B., Plasterk, R.H., Ketting, R.F., and Hannon, G.J. (2004). Processing of primary microRNAs by the microprocessor complex. Nature *432*, 231–235. https://doi.org/10.1038/nature03049.

DeVeale, B., Swindlehurst-Chan, J., and Blelloch, R. (2021). The roles of microRNAs in mouse development. Nat. Rev. Genet. *22*, 307–323. https://doi.org/10.1038/s41576-020-00309-5.

Dika, E., Broseghini, E., Porcellini, E., Lambertini, M., Riefolo, M., Durante, G., Loher, P., Roncarati, R., Bassi, C., Misciali, C., et al. (2021). Unraveling the role of microRNA/isomiR network in multiple primary melanoma pathogenesis. Cell Death Dis. *12*, 473. https://doi.org/10.1038/s41419-021-03764-y.

Du, P., Pirouz, M., Choi, J., Huebner, A.J., Clement, K., Meissner, A., Hochedlinger, K., and Gregory, R.I. (2018). An intermediate pluripotent state controlled by microRNAs is required for the naive-to-primed stem cell transition. Cell Stem Cell *22*, 851–864.e5. https://doi.org/10.1016/j.stem.2018.04.021.

Du, P., Wu, J., Zhang, J., Zhao, S., Zheng, H., Gao, G., Wei, L., and Li, Y. (2011). Viral infection induces expression of novel phased microRNAs from conserved cellular microRNA precursors. PLoS Pathog. *7*, e1002176. https://doi.org/10.1371/journal.ppat.1002176.

Fire, A., Xu, S., Montgomery, M.K., Kostas, S.A., Driver, S.E., and Mello, C.C. (1998). Potent and specific genetic interference by double-stranded RNA in *Caenorhabditis elegans*. Nature *391*, 806–811. https://doi.org/10.1038/35888.

Gaur, A., Jewell, D.A., Liang, Y., Ridzon, D., Moore, J.H., Chen, C., Ambros, V.R., and Israel, M.A. (2007). Characterization of microRNA expression levels and their biological correlates in human cancer cell lines. Cancer Res. *67*, 2456–2468. https://doi.org/10.1158/0008-5472.CAN-06-2698.

Gregory, R.I., Yan, K.P., Amuthan, G., Chendrimada, T., Doratotaj, B., Cooch, N., and Shiekhattar, R. (2004). The microprocessor complex mediates the genesis of microRNAs. Nature *432*, 235–240. https://doi.org/10.1038/nature03120.

Guo, Z., Li, Y., and Ding, S.W. (2019). Small RNA-based antimicrobial immunity. Nat. Rev. Immunol. *19*, 31–44. https://doi.org/10.1038/s41577-018-0071-x.

Hammond, S.M., Bernstein, E., Beach, D., and Hannon, G.J. (2000). An RNA-directed nuclease mediates post-transcriptional gene silencing in Drosophila cells. Nature *404*, 293–296. https://doi.org/10.1038/35005107.

Hanahan, D., and Weinberg, R.A. (2011). Hallmarks of cancer: the next generation. Cell *144*, 646–674. https://doi.org/10.1016/j.cell.2011.02.013.

Heo, I., Ha, M., Lim, J., Yoon, M.J., Park, J.E., Kwon, S.C., Chang, H., and Kim, V.N. (2012). Mono-uridylation of pre-microRNA as a key step in the biogenesis of group II let-7 microRNAs. Cell *151*, 521–532. https://doi.org/10.1016/j.cell.2012.09.022.

Holohan, C., Van Schaeybroeck, S., Longley, D.B., and Johnston, P.G. (2013). Cancer drug resistance: an evolving paradigm. Nat. Rev. Cancer *13*, 714–726. https://doi.org/10.1038/nrc3599.

Hydbring, P., Wang, Y., Fassl, A., Li, X., Matia, V., Otto, T., Choi, Y.J., Sweeney, K.E., Suski, J.M., Yin, H., et al. (2017). Cell-cycle-targeting microRNAs as therapeutic tools against refractory cancers. Cancer Cell *31*, 576–590.e8. https://doi.org/10.1016/j.ccell.2017.03.004.

Jinek, M., Chylinski, K., Fonfara, I., Hauer, M., Doudna, J.A., and Charpentier, E. (2012). A programmable dual-RNA-guided DNA endonuclease in adaptive bacterial immunity. Science *337*, 816–821. https://doi.org/10.1126/science.1225829.

Katoh, T., Sakaguchi, Y., Miyauchi, K., Suzuki, T., Kashiwabara, S.-i., Baba, T., and Suzuki, T. (2009). Selective stabilization of mammalian microRNAs by 3′ adenylation mediated by the cytoplasmic poly (A) polymerase GLD-2. Genes Dev. *23*, 433–438.

Kim, D., Langmead, B., and Salzberg, S.L. (2015). HISAT: a fast spliced aligner with low memory requirements. Nat. Methods *12*, 357–360. https://doi.org/10.1038/nmeth.3317.

Lambo, S., Gröbner, S.N., Rausch, T., Waszak, S.M., Schmidt, C., Gorthi, A., Romero, J.C., Mauermann, M., Brabetz, S., Krausert, S., et al. (2019). The molecular landscape of ETMR at diagnosis and relapse. Nature *576*, 274–280. https://doi.org/10.1038/s41586-019-1815-x.

Langmead, B., Trapnell, C., Pop, M., and Salzberg, S.L. (2009). Ultrafast and memory-efficient alignment of short DNA sequences to the human genome. Genome Biol. *10*, R25. https://doi.org/10.1186/gb-2009-10-3-r25.

Lee, R.C., Feinbaum, R.L., and Ambros, V. (1993). The *C. elegans* heterochronic gene lin-4 encodes small RNAs with antisense complementarity to lin-14. Cell *75*, 843–854. https://doi.org/10.1016/0092-8674(93)90529-Y.

Lee, Y., Ahn, C., Han, J., Choi, H., Kim, J., Yim, J., Lee, J., Provost, P., Rådmark, O., Kim, S., and Kim, V.N. (2003). The nuclear RNase III Drosha initiates microRNA processing. Nature *425*, 415–419. https://doi.org/10.1038/nature01957.

Liao, Y., Smyth, G.K., and Shi, W. (2014). featureCounts: an efficient general purpose program for assigning sequence reads to genomic features. Bioinformatics *30*, 923–930. https://doi.org/10.1093/bioinformatics/btt656.

Lin, S., and Gregory, R.I. (2015). MicroRNA biogenesis pathways in cancer. Nat. Rev. Cancer *15*, 321–333. https://doi.org/10.1038/nrc3932.

Lu, J., Getz, G., Miska, E.A., Alvarez-Saavedra, E., Lamb, J., Peck, D., Sweet-Cordero, A., Ebert, B.L., Mak, R.H., Ferrando, A.A., et al. (2005). MicroRNA

expression profiles classify human cancers. Nature *435*, 834–838. https://doi.org/10.1038/nature03702.

Ma, J.B., Ye, K., and Patel, D.J. (2004). Structural basis for overhang-specific small interfering RNA recognition by the PAZ domain. Nature *429*, 318–322.

Mali, P., Yang, L., Esvelt, K.M., Aach, J., Guell, M., DiCarlo, J.E., Norville, J.E., and Church, G.M. (2013). RNA-guided human genome engineering via Cas9. Science *339*, 823–826. https://doi.org/10.1126/science.1232033.

Malumbres, M., and Barbacid, M. (2009). Cell cycle, CDKs and cancer: a changing paradigm. Nat. Rev. Cancer *9*, 153–166. https://doi.org/10.1038/nrc2602.

McCall, M.N., Kim, M.-S., Adil, M., Patil, A.H., Lu, Y., Mitchell, C.J., Leal-Rojas, P., Xu, J., Kumar, M., Dawson, V.L., et al. (2017). Toward the human cellular microRNAome. Genome Res. *27*, 1769–1781.

Meister, G., and Tuschl, T. (2004). Mechanisms of gene silencing by double-stranded RNA. Nature *431*, 343–349. https://doi.org/10.1038/nature02873.

Moazed, D. (2009). Small RNAs in transcriptional gene silencing and genome defence. Nature *457*, 413–420. https://doi.org/10.1038/nature07756.

Mootha, V.K., Lindgren, C.M., Eriksson, K.-F., Subramanian, A., Sihag, S., Lehar, J., Puigserver, P., Carlsson, E., Ridderstråle, M., Laurila, E., et al. (2003). PGC-1α-responsive genes involved in oxidative phosphorylation are coordinately downregulated in human diabetes. Nat. Genet. *34*, 267–273. https://doi.org/10.1038/ng1180.

Otto, T., and Sicinski, P. (2017). Cell cycle proteins as promising targets in cancer therapy. Nat. Rev. Cancer *17*, 93–115. https://doi.org/10.1038/nrc.2016.138.

Ramírez-Moya, J., Wert-Lamas, L., Riesco-Eizaguirre, G., and Santisteban, P. (2019). Impaired microRNA processing by DICER1 downregulation endows thyroid cancer with increased aggressiveness. Oncogene *38*, 5486–5499. https://doi.org/10.1038/s41388-019-0804-8.

Rupaimoole, R., and Slack, F.J. (2017). MicroRNA therapeutics: towards a new era for the management of cancer and other diseases. Nat. Rev. Drug Discov. *16*, 203–222. https://doi.org/10.1038/nrd.2016.246.

Sharma, G., Sharma, A.R., Bhattacharya, M., Lee, S.S., and Chakraborty, C. (2021). CRISPR-Cas9: a preclinical and clinical perspective for the treatment of human diseases. Mol. Ther. *29*, 571–586. https://doi.org/10.1016/j.ymthe.2020.09.028.

Sheu-Gruttadauria, J., Pawlica, P., Klum, S.M., Wang, S., Yario, T.A., Schirle Oakdale, N.T., Steitz, J.A., and MacRae, I.J. (2019). Structural basis for target-directed microRNA degradation. Mol. Cell *75*, 1243–1255.e7. https://doi.org/10.1016/j.molcel.2019.06.019.

Slack, F.J., and Chinnaiyan, A.M. (2019). The role of non-coding RNAs in oncology. Cell *179*, 1033–1055. https://doi.org/10.1016/j.cell.2019.10.017.

Stuart, T., Butler, A., Hoffman, P., Hafemeister, C., Papalexi, E., Mauck, W.M., Hao, Y., Stoeckius, M., Smibert, P., and Satija, R. (2019). Comprehensive integration of single-cell data. Cell *177*, 1888–1902.e21. https://doi.org/10.1016/j.cell.2019.05.031.

Subramanian, A., Tamayo, P., Mootha, V.K., Mukherjee, S., Ebert, B.L., Gillette, M.A., Paulovich, A., Pomeroy, S.L., Golub, T.R., Lander, E.S., and Mesirov, J.P. (2005). Gene set enrichment analysis: a knowledge-based approach for interpreting genome-wide expression profiles. Proc. Natl. Acad. Sci. USA *102*, 15545–15550. https://doi.org/10.1073/pnas.0506580102.

Sun, H.L., Cui, R., Zhou, J., Teng, K.Y., Hsiao, Y.H., Nakanishi, K., Fassan, M., Luo, Z., Shi, G., Tili, E., et al. (2016). ERK activation globally downregulates miRNAs through phosphorylating Exportin-5. Cancer Cell *30*, 723–736. https://doi.org/10.1016/j.ccell.2016.10.001.

Suski, J.M., Braun, M., Strmiska, V., and Sicinski, P. (2021). Targeting cell-cycle machinery in cancer. Cancer Cell *39*, 759–778. https://doi.org/10.1016/j.ccell.2021.03.010.

Thomson, J.M., Newman, M., Parker, J.S., Morin-Kensicki, E.M., Wright, T., and Hammond, S.M. (2006). Extensive post-transcriptional regulation of microRNAs and its implications for cancer. Genes Dev. *20*, 2202–2207. https://doi.org/10.1101/gad.1444406.

Thornton, J.E., Du, P., Jing, L., Sjekloca, L., Lin, S., Grossi, E., Sliz, P., Zon, L.I., and Gregory, R.I. (2014). Selective microRNA uridylation by Zcchc6 (TUT7) and Zcchc11 (TUT4). Nucleic Acids Res. *42*, 11777–11791. https://doi.org/10.1093/nar/gku805.

Tu, B., Liu, L., Xu, C., Zhai, J., Li, S., Lopez, M.A., Zhao, Y., Yu, Y., Ramachandran, V., Ren, G., et al. (2015). Distinct and cooperative activities of HESO1 and URT1 nucleotidyl transferases in microRNA turnover in Arabidopsis. PLoS Genet. *11*, e1005119. https://doi.org/10.1371/journal.pgen.1005119.

Walz, A.L., Ooms, A., Gadd, S., Gerhard, D.S., Smith, M.A., Guidry Auvil, J.M., Meerzaman, D., Chen, Q.R., Hsu, C.H., Yan, C., et al. (2015). Recurrent DGCR8, DROSHA, and SIX homeodomain mutations in favorable histology Wilms tumors. Cancer Cell *27*, 286–297. https://doi.org/10.1016/j.ccell.2015.01.003.

Wang, D., Tai, P.W.L., and Gao, G. (2019). Adeno-associated virus vector as a platform for gene therapy delivery. Nat. Rev. Drug Discov. *18*, 358–378. https://doi.org/10.1038/s41573-019-0012-9.

Wightman, B., Ha, I., and Ruvkun, G. (1993). Posttranscriptional regulation of the heterochronic gene lin-14 by lin-4 mediates temporal pattern formation in *C. elegans*. Cell *75*, 855–862. https://doi.org/10.1016/0092-8674(93)90530-4.

Yu, S., and Kim, V.N. (2020). A tale of non-canonical tails: gene regulation by post-transcriptional RNA tailing. Nat. Rev. Mol. Cell Biol. *21*, 542–556. https://doi.org/10.1038/s41580-020-0246-8.

Zamore, P.D., Tuschl, T., Sharp, P.A., and Bartel, D.P. (2000). RNAi: double-stranded RNA directs the ATP-dependent cleavage of mRNA at 21 to 23 nucleotide intervals. Cell *101*, 25–33. https://doi.org/10.1016/S0092-8674(00)80620-0.

Zong, J., Yao, X., Yin, J., Zhang, D., and Ma, H. (2009). Evolution of the RNA-dependent RNA polymerase (RdRP) genes: duplications and possible losses before and after the divergence of major eukaryotic groups. Gene *447*, 29–39. https://doi.org/10.1016/j.gene.2009.07.004.

STAR★METHODS

KEY RESOURCES TABLE

REAGENT or RESOURCE	SOURCE	IDENTIFIER
Antibodies		
Monoclonal ANTI-FLAG® M2-Peroxidase (HRP) antibody	Sigma	Cat# A8592; RRID:AB_439702
Anti-Plk Antibody (F-8)	Santa Cruz Biotechnology	Cat# sc-17783; RRID:AB_628157
Anti-Myc Tag, clone 4A6 antibody	Millipore	Cat# 05-724; RRID:AB_309938
Monoclonal mouse anti-human Ago2	Abnova	Cat# H00027161-M01; RRID:AB_2277660
ACTB Monoclonal Antibody	ABclonal	Cat# AC004; RRID:AB_2737399
HRP-conjugated Mouse anti His-Tag mAb antibody	ABclonal	Cat# AE028; RRID: AB_2769867
Mouse anti GFP-Tag mAb antibody	ABclonal	Cat# AE012; RRID:AB_ 2862747
Argonaute-2 Rabbit mAb antibody	ABclonal	Cat# A19709; RRID:AB_2576208
Cyclin D1 Rabbit mAb antibody	ABclonal	Cat# A19038; RRID: AB_2862530
CCNE2 Polyclonal Antibody	ABclonal	Cat# A7032; RRID: AB_2767587
CDK6 Rabbit pAb antibody	ABclonal	Cat# A1545; RRID: AB_2861718
MCM2 Polyclonal Antibody	ABclonal	Cat# A1056; RRID: AB_2758102
HRP Goat Anti-Mouse IgG (H+L)	Biodragon	Cat# BF03001;
HRP Goat Anti-Rabbit IgG (H+L)	Biodragon	Cat# BF03008;
Bacterial and virus strains		
Stbl3 Competent Cell	Tsingke	Cat# TSC06
*Trans*etta (DE3) Cell	Transgen	Cat# CD801
pTRE-EGFP	N/A	N/A
pLVX-Tet3G	N/A	N/A
psPAX2	N/A	N/A
pMD2.G	N/A	N/A
pTRE-AtRDR1-T2A-EGFP	This paper	N/A
pTRE-OsRDR1-T2A-EGFP	This paper	N/A
pSIN-EGFP	N/A	N/A
pSIN-MYC-AGO2	This paper	N/A
pSIN-OsRDR1-T2A-EGFP	This paper	N/A
pTRE-RDR1-Mut-T2A-EGFP	This paper	N/A
pTRE-mCherry-OsRDR1-T2A-EGFP	This paper	N/A
pTRE-OsRDR1	This paper	N/A
AAV-CAG-EGFP	N/A	N/A
AAV-CAG-FLAG-OsRDR1	This paper	N/A
Chemicals, peptides, and recombinant proteins		
DMEM	Gibco	Cat# 11965092
RPMI-1640	Gibco	Cat# 11875101
Opti-MEM™ I Reduced Serum Medium	Gibco	Cat# 31985070
L-Glutamine	Gibco	Cat# 25030081
Sodium Pyruvate	Gibco	Cat# 11360070

(*Continued on next page*)

Continued

REAGENT or RESOURCE	SOURCE	IDENTIFIER
Penicillin-Streptomycin	Gibco	Cat# 15140163
Non-Essential Amino Acids Solution (NEAA)	Gibco	Cat# 11140050
Sodium Pyruvate	Gibco	Cat# 11360070
Geneticin	Gibco	Cat# 10131027
Trypsin-EDTA	Gibco	Cat# 15400054
0.25% non-EDTA trypsin	Gibco	Cat# 15050057
DPBS	Gibco	Cat# 14190250
Essential 8 medium	Cellapy	Cat# CA1014500
Fetal Bovine Serum	Gemini	Cat# 900-108
Gelatin from porcine skin	Sigma	Cat# G1890
Bovine Serum Albumin	Sigma	Cat# B2064
Chloroform	Sigma	Cat# C2432-500ML
Dimethyl sulfoxide	Sigma	Cat# D2650
Doxycycline hyclate	Sigma	Cat# D9891
DTT	Sigma	Cat# D0632
EDC	Sigma	Cat# E7750
Imidazole	Sigma	Cat# I2399
PerfectHyb™ Plus hybridization buffer	Sigma	Cat# H7033
Polyethyleneimine	Sigma	Cat# 919012
Protease Inhibitor Cocktail	Sigma	Cat# P8849
Puromycin	Sigma	Cat# 540411
Triton X-100	Sigma	Cat# X100-500ML
Mouse Leukemia Inhibitory Factor (LIF)	Millipore	Cat# ESG1107
Matrigel hESC-Qualified Matrix	Corning	Cat# 354277
Palbociclib	Selleck	Cat# S4482
2-Mercaptoethanol	ThermoFisher	Cat# 60-24-2
ATP	ThermoFisher	Cat# R0441
NuPAGE™ LDS Sample Buffer (4X)	ThermoFisher	Cat# NP0007
Ampicillin	Sangon biotech	Cat# B541011
Chloramphenicol	Sangon biotech	Cat# B541015
Isopropyl β-D-Thiogalactoside	Sangon biotech	Cat# B541007
BeyoECL Plus	Beyotime	Cat# P0018A
D-Luciferin	Beyotime	Cat# ST198
PMSF	Beyotime	Cat# ST506
Lipofectamine™ 3000 Transfection Reagent	Invitrogen	Cat# 11668019
Proteinase K	Invitrogen	Cat# 25530015
TRIzol™ Reagent	Invitrogen	Cat# 15596026
UltraPure™ DNase/RNase-Free Distilled Water	Invitrogen	Cat# 10977015
DNase I	New England Biolabs	Cat# M0303
E. coli Poly(A) Polymerase	New England Biolabs	Cat# M0276
M-MuLV reverse transcriptase	New England Biolabs	Cat# M0253
2X RNA Loading Dye	New England Biolabs	Cat# B0363S
T4 Polynucleotide Kinase	New England Biolabs	Cat# M0201L
T4 RNA Ligase 1 (ssRNA Ligase, high concentration)	New England Biolabs	Cat# M0437M
T4 ligase reaction buffer	New England Biolabs	Cat# B0216S

(*Continued on next page*)

Continued

REAGENT or RESOURCE	SOURCE	IDENTIFIER
Rnasin	Promega	Cat# N2518
Lysing buffer	BD Pharmingen	Cat# 555899
0.1% crystal violet	Solarbio	Cat# G1063
DAPI solution (ready-to-use)	Solarbio	Cat# C0065
Propidium iodide	Solarbio	Cat# C0080
Polybrene	Solarbio	Cat# H8761
4% Paraformaldehyde Fix Solution (PFA)	BBI Life Science	Cat# E672002-0100
0.4% trypan blue staining solution	Coolaber	Cat# SL7120
Argonaute-2 Protein, Human, Recombinant (His Tag)	Sino Biological	Cat# 11079-H07B
Critical commercial assays		
TruSeq Stranded mRNA Sample Prep Kits	Illumina	Cat# RS-122-2101
Q5 High-Fidelity 2X Master Mix	New England Biolabs	Cat# M0492S
Q5 Site-Directed Mutagenesis Kit	New England Biolabs	Cat# E0554
Gibson Assembly Master Mix	New England Biolabs	Cat# E2611S
NEBNext® Small RNA Library Prep Set for Illumina kit	New England Biolabs	Cat# E7580L
SuperScript IV RT kit	Invitrogen	Cat# 18090010
Novex™ TBE-Urea Gels, 15%, 10 well	Invitrogen	Cat# EC6885BOX
Protein A Dynabeads	Life Technologies	Cat# 10001D
Annexin V-PE/7-AAD kit	Vazyme	Cat# A213
VAHTS Stranded mRNA-seq Library Prep Kits	Vazyme	Cat# NR602
Ribo-off Globin & rRNA Depletion Kit (Human/Mouse/Rat)	Vazyme	Cat# N408
Chromium Next GEM Single Cell 3' Kit v3.1	10x Genomics	Cat# PN-1000268
Chromium Single Cell A Chip Kit	10x Genomics	Cat# PN-120236
Chromium i7 Multiplex Kit	10x Genomics	Cat# PN-120262
DNA Clean & Concentrator Kits	Zymo	Cat# DP4033
RNA Clean & Concentrator Kits	Zymo	Cat# R1017
SurePAGE™, Bis-Tris, 10x8, 4-12%, 15 wells	Genscript	Cat# M00654
2X M5 HiPer Realtime PCR Super mix	Mei5bio	Cat# MF013
Immobilon-P Membrane, PVDF, 0.45 mm	Millipore	Cat# IPVH07850
BeyoClick™ EdU Cell Proliferation Kit with Alexa Fluor 488	Beyotime	Cat# C0071
IDA-Ni Beads	Beaverbio	Cat# 70501-5
PULSin	Polyplus-transfection	Cat# PT-501-04
BioCoat Matrigel Invasion Chamber	Corning	Cat# 354480
TransDetect® Double-Luciferase Reporter Assay Kit	Transgen	Cat# FR201
Deposited data		
RNA-seq & small RNA-seq	This study	GEO: GSE198147
TCGA isoform expression quantification data	The Genomic Data Commons (GDC)	https://gdc.cancer.gov/about-data/publications/pancanatlas
Small RNA-seq of primary human cells	(McCall et al., 2017)	N/A

(*Continued on next page*)

Continued

REAGENT or RESOURCE	SOURCE	IDENTIFIER
Additional small RNA-seq datasets	Gene Expression Omnibus; https://www.ncbi.nlm.nih.gov/geo/	GEO: GSE60292; GEO: GSE62913; GEO: GSE68189; GEO: GSE33665; GEO: GSE39162; GEO: GSE24457; GEO: GSE37616; GEO: GSE21279; GEO: GSE16579; GEO: GSE51507; GEO: GSE58127; GEO: GSE59944; GEO: GSE60036; GEO: GSE64422; GEO: GSE66823; GEO: GSE47534; GEO: GSE50429
Additional small RNA-seq datasets	Sequence Read Archive (SRA); https://www.ncbi.nlm.nih.gov/sra/	DRX000313; ERX202577; ERX344647; SRX201519
Experimental models: Cell lines		
Human cell line: A549	Beijing Vitalstar Biotechnology	N/A
Human cell line: HCT116	N/A	N/A
Human cell line: HepG2	N/A	N/A
Human cell line: HeLa	N/A	N/A
Human cell line: H1299	N/A	N/A
Human cell line: PC-3	Beijing Vitalstar Biotechnology	N/A
Human cell line: U-2 OS	Gift from Jiazhi Hu	N/A
Human cell line: Jurkat	Beijing Vitalstar Biotechnology	N/A
Human cell line: K562	Gift from Sherry Lee	N/A
Human cell line: NALM6	Beijing Vitalstar Biotechnology	N/A
Human cell line: RPE-1	N/A	N/A
Human cell line: HEK293T	N/A	N/A
Human cell line: WPMY-1	N/A	N/A
Human cell line: WIBR3 ES cells	N/A	N/A
Mouse cell line: NIH/3T3	N/A	N/A
Mouse cell line: V6.5 ES cells	N/A	N/A
Experimental models: Organisms/strains		
NPG (NOD.Cg-*Prkdc*^{scid}*Il2rg*^{tm1Vst}/Vst) mice	Beijing Vitalstar Biotechnology	Stock No: VS-AM-001
NOG (NOD.Cg-*Prkdc*^{scid}*Il2rg*^{tm1Sug}/JicCrl) mice	Beijing Vital River Laboratory Animal Technology	Stock No: 408
Oligonucleotides		
Primers for qPCR, see Table S7	This study	N/A
siRNA targeting sequence, see Table S7	This study	RIBOBIO
Recombinant DNA		
psiCHECK2	Promega	Cat# C8021
psiCHECK2-CCNE1	This paper	N/A
psiCHECK2-CCNE1-Mut	This paper	N/A
psiCHECK2-CDK6	This paper	N/A
psiCHECK2-CDK6-Mut	This paper	N/A
psiCHECK2-CDC25A	This paper	N/A
pETDuet-1	N/A	N/A
pETDuet-AtRDR1	This paper	N/A
pETDuet-AtRDR1-Mut	This paper	N/A
Software and algorithms		
ImageJ (Fiji)	NIH	RRID: SCR_0030.70
GraphPad Prism7	GraphPad Software	N/A

(*Continued on next page*)

Continued

REAGENT or RESOURCE	SOURCE	IDENTIFIER
Trimmomatic 0.39	(Bolger et al., 2014)	http://www.usadellab.org/cms/?page=trimmomatic
FastQC 0.11.8	The Babraham Bioinformatics group	https://www.bioinformatics.babraham.ac.uk/projects/fastqc/
HISAT2 2.1.0	(Kim et al., 2015)	http://daehwankimlab.github.io/hisat2/
FeatureCounts 1.6.4	(Liao et al., 2014)	http://bioinf.wehi.edu.au/featureCounts/
GSEA 4.1.0	(Mootha et al., 2003; Subramanian et al., 2005)	http://www.gsea-msigdb.org/gsea/
Cytoscape 3.8.2	National Resource for Network Biology	https://cytoscape.org/
Perl 5.26.2	The Perl Foundation	https://www.perl.org/
Python 3.8.5	The Python Software Foundation	https://www.python.org/
R 3.5.1	The R Foundation for Statistical Computing	https://www.r-project.org/
Bowtie 1.0.0	(Langmead et al., 2009)	http://bowtie-bio.sourceforge.net/manual.shtml
Cellranger 5.0.1	10x Genomics	https://support.10xgenomics.com/single-cell-gene-expression/software/downloads/latest
Seurat 3.2.3	(Stuart et al., 2019)	https://satijalab.org/seurat/
BioRender	BioRender	https://biorender.com/

RESOURCE AVAILABILITY

Lead contact

Further queries and reagent requests may be directed and will be fulfilled by the lead contact, Peng Du (pengdu@pku.edu.cn).

Materials availability

Plasmids and cell lines generated in this study are available from the lead contact with a completed Materials Transfer Agreement.

Data and code availability

The RNA-seq and small RNA-seq data generated during this study are available at GEO: GSE198147.

EXPERIMENTAL MODEL AND SUBJECT DETAILS

Mice

All animal experiments were performed according to the Animal Protection Guidelines of Peking University, China. NOD.Cg-*Prkdc*^{scid} *Il2rg*^{tm1Vst}/Vst (NPG) and NOD.Cg-*Prkdc*^{scid}*Il2rg*^{tm1Sug}/JicCrl (NOG) mice were purchased from Beijing Vitalstar Biotechnology and Beijing Vital River Laboratory Animal Technology, respectively. Mice were fed regular chow and housed in a pathogen-free animal facility under a 12:12-hour light-dark cycle at 22°C in Beijing Vitalstar Laboratory and Beijing Vital River Laboratory. Xenograft experiments were performed on 4-6 weeks old mice. Female mice were used for all cancer models except PC-3 xenograft models. For doxycycline (Dox)-regulated RDR1 induction, Dox-containing drinking water was provided to the mice (1 mg/ml, Sigma D9891).

Cell culture

All mouse and human cell lines were cultured at 37°C with 20% (v/v) O_2 and 5% (v/v) CO_2. Solid tumor cell lines (A549, HCT116, HeLa, HepG2, H1299, PC-3 and U-2 OS), HEK293T, NIH/3T3 and RPE-1) were cultured with DMEM (Gibco, 11965092) supplemented with 10% (v/v) FBS (Gemini, 900-108), 2 mM L-glutamine (Gibco, 25030081), 50 μM 2-mercaptoethanol (ThermoFisher, 60-24-2) and 1% (v/v) penicillin-streptomycin (Gibco, 15140163). Leukemia cell lines (Jurkat, K562 and NALM6) were cultured in RPMI 1640 (Gibco, 11875101) with 10% (v/v) FBS (Gemini, 900-108) and 1% penicillin-streptomycin (Gibco, 15140163). V6.5 cell line was cultured on 0.2% gelatin (Sigma, G1890) in Serum/LIF medium composed of DMEM (Gibco, 11965092), 15% FBS (Gibco, 1009914), 2 mM L-glutamine (Gibco, 25030081), 1% (v/v) penicillin-streptomycin (Gibco, 15140163), 1X non-essential amino acids (NEAA) (Gibco, 11140050), 1X sodium pyruvate (Gibco, 11360070), 50 μM 2-mercaptoethanol (ThermoFisher, 60-24-2) and 1000 U/ml mouse leukemia inhibitory factor (mLIF) (Millipore, ESG1107). Primed ESC cell line WIBR3 was grown on matrigel (Corning, 354277) and

cultured in Essential 8 medium (Cellapy, CA1014500). Cells were passaged using 0.5 mM EDTA every 3-6 days at a split ratio of 1:3-1:6.

All Dox-inducible cell lines expressing AtRDR1 or OsRDR1 were cultured with the same medium as described above supplemented with 100 ng/ml Dox (low concentration) before cell sorting or 4 μg/ml Dox (high concentration) to induce RDR1 expression. Dox was replenished every day.

METHOD DETAILS

Generation of stable cell lines

To generate stable cell lines with Dox-inducible RDR1 expression, plant AtRDR1 and OsRDR1 cDNA were generated using SuperScript IV RT kit (Invitrogen, 18090010). AtRDR1 and OsRDR1 were FLAG-tagged and then cloned into pTRE-EGFP lentiviral vector with the T2A-EGFP fragment using Gibson Assembly Master Mix (NEB, E2611S). To generate lentiviral particles, pTRE-RDR1-T2A-EGFP or pLVX-Tet3G together with psPAX2 and pMD2.G plasmids were co-transfected into 293T cells using Lipofectamine™ 3000 (Invitrogen, 11668019) according to the manufacturer's instructions. The lentivirus was harvested 51 h after transfection. Different cell lines were then transduced by incubating with the appropriate volume of lentiviral particles in the presence of 8 μg/ml polybrene (Solarbio, H8761) for 24 h. Thereafter, 100 ng/ml Dox was added to the medium for 24 h. Next, EGFP+ cells were sorted using BD FACSAria™ III to obtain stable cell lines with inducible expression of plant RDR1.

To generate stable cell lines with consistent RDR1 expression, OsRDR1-T2A-EGFP fragment was amplified by PCR and cloned into the EcoRI and BamHI sites of pSIN-EGFP vector. The steps of generating lentiviral particles were described above. For V6.5, EGFP+ cells were sorted by flow cytometry and then expanded. For WIBR3, 1 μg/ml puromycin (Sigma, 540411) was used to select positive cells before sorting by flow cytometry.

To generate stable cell lines with human AGO2 overexpression, MYC-AGO2 fragment was amplified by PCR and cloned into the EcoRI and BamHI sites of pSIN-EGFP vector. The steps of generating lentiviral particles were described above. After 48 h of infection, 2 μg/ml puromycin was used to select cells with MYC-AGO2 overexpression for 2 days.

To generate stable cell lines with catalytic mutant RDR1 expression, Q5 Site-Directed Mutagenesis Kit (NEB, E0554) was used to generate the OsRDR1 mutant, of which the 430th, 432nd, 434th aspartates were substituted by alanine. The remaining steps were similar to those for generating RDR1 stable cell lines.

Western blot

For immunoblotting, cells were lysed in cold lysis buffer (20 mM Tris-HCl [pH7.6], 137 mM NaCl, 1 mM EDTA, 1% Triton X-100, 1.5 mM $MgCl_2$) supplemented with 1 mM PMSF (Beyotime, ST506), and then mixed with 4 x NuPAGE™ LDS sample buffer (Invitrogen, NP0007) before incubating at 98°C for 10 min. Subsequently, the protein samples were loaded for SDS-PAGE and transferred to PVDF membranes (Millipore, IPVH07850) using a Bio-Rad transfer apparatus. The membrane was blocked with 5% non-fat milk in TBS containing 0.1% Tween-20 (TBST) at room temperature for 2 h, followed by incubation with primary antibody overnight at 4°C. Following three 10 min washes with TBST, membranes were incubated with species-specific secondary antibodies at room temperature for 1 h while shaking. After three 10 min washes in TBST, the membrane was detected by Western ECL substrate and imaged with Amersham Imager 600 (GE Healthcare). The following primary antibodies were used: anti-ACTIN (1:5000, ABclonal, AC004), anti-FLAG® M2-Peroxidase (HRP) (1:3000, Sigma, A8592), anti-HIS (1:2000, ABclonal, AE028), anti-MYC (1:3000, Millipore, 05-724), anti-GFP (1:2000, ABclonal, AE012), anti-AGO2 (1:2000, ABclonal, A19709), anti-CCND1 (1:2000, ABclonal, A19038), anti-CCNE2 (1:2000, ABclonal, A7032), anti-CDK6 (1:2000, ABclonal, A1545), anti-MCM2 (1:2000, ABclonal, A1056) and anti-PLK1 (1:2000, Santa Cruz Biotechnology, sc-17783).

RDR1 localization

The mCherry fragment was PCR amplified and cloned into pTRE-EGFP lentiviral vector with FLAG-OsRDR1 and T2A-EGFP fragments by using Gibson Assembly Master Mix to research the location of RDR1 in living cells. Lentiviral particles were prepared as described above and viral transductions were performed in the presence of 8 μg/ml polybrene. Similarly, 100 ng/ml Dox was added to the medium for 24 h and EGFP+/mCherry+ cells were sorted by flow cytometry. To detect the localization of RDR1 in living cells, the medium containing 4 μg/ml Dox is used to induce mCherry-OsRDR1 expression for 60 h. After washing the cells twice with PBS, the cells were incubated with 1 μg/ml DAPI (Solarbio, C0065) at room temperature for 30 min. The imaging was performed using Nikon A1RSi+ Confocal microscope with 100× oil immersion objective in a live cell imaging chamber.

Cell proliferation assay

Different cancer cell lines or non-cancer control cell lines were seeded in 12-well plates at 10,000 cells per well on day 0. For RDR1-inducible cell lines, dox (4 μg/ml) was added to the culture medium and replenished every day. After digestion, cells were stained with 0.4% trypan blue staining solution (Coolaber, SL7120) and counted using Coulter Counter. The number of cells was measured at a fixed time for 5-6 days.

Colony formation

In six-well culture dishes, 500 cells were seeded per well in the presence or absence of Dox (4 μg/ml). After 7 days, the culture medium was removed and the cells were washed twice with PBS, fixed in 4% paraformaldehyde (PFA) at room temperature for 30 min, stained with 0.1% crystal violet (Solarbio, G1063) for 30 min, washed with pure water and dried. Colonies were counted manually.

Wound healing assay and cell invasion assay

Before wound healing assay and cell invasion assay, medium that contained 4 μg/ml Dox was used to induce RDR1 expression for 72 h. In wound healing assay, cells were seeded in culture-inserts (ibidi, 81167) at a density of 40,000 cells per well in the presence or absence of Dox (4 μg/ml). After 24 h, the culture-insert was gently removed and the cell layer was washed with PBS to remove cell debris and non-attached cells. The μ-Dish was filled with serum-free medium to prevent cell proliferation and induce migration. Cells were imaged directly after removing the culture-insert and 18 h later. The relative distance and areas were quantified using image J.

Cell invasion was measured using BioCoat Matrigel Invasion Chamber (Corning, 354480) following the manufacturer's instructions. Briefly, inserts were rehydrated with Opti-MEM (Gibco, 31985070) for 2 h in humidified cell culture incubator. In each insert, 30,000 cells were seeded in DMEM basic medium. Complete medium described above was added in the lower chamber. After 18 h invasion, cells in the lower surface of the chamber were fixed in 4% PFA at room temperature for 30 min, visualized with 0.1% crystal violet for 30 min. Invasion cells were counted manually.

EdU/PI staining

Q5 Site-Directed Mutagenesis Kit was used to delete the T2A-EGFP fragment in pTRE-RDR1-T2A-EGFP vector. Lentiviral particles were prepared as described above and 100 × Geneticin (Gibco, 10131027) was used to obtain RDR1 cell lines without EGFP expression. Six days after induction of RDR1 expression, cell cycle stage was determined using BeyoClick™ EdU Cell Proliferation Kit with Alexa Fluor 488 (Beyotime, C0071) according to the manufacturer's instructions. Briefly, cells were incubated with EdU (10 μM final concentration) for 120 min, digested using 0.25% trypsin-EDTA, fixed in 4% PFA followed by permeabilization in PBS/0.3% Triton X-100 at room temperature for 15 min. After washing three times in washing buffer (PBS/3% BSA), click reaction solution was added to the tube and incubated in the dark for 30 min at room temperature. Next, the cell suspension was washed in washing solution and counterstained with propidium iodide (PI) (Solarbio, C0080) diluted in PBS with RNase. The samples were analyzed on a Beckman CytoFLEX S device.

For cell cycle inhibition and small RNA-seq assay, HeLa cells were incubated for 48 h with 0.5 μM palbociclib (Selleck, S4482) or DMSO and harvested for EdU/PI staining or small RNA-seq assay. The method of staining and detection of the cell cycle stage is the same as above.

Total RNA extraction and q.RT-PCR

TRIzol reagent (Invitrogen, 15596026) was used to isolate total RNA from cells or tumor tissues according to the manufacturer's instructions. For miRNA qRT-PCR, 500 ng or 1 μg of total RNA was treated with DNase I (NEB, M0303) to remove genomic DNA and *E. coli* Poly(A) Polymerase (NEB, M0276) to add poly(A) tail to RNA. M-MuLV reverse transcriptase (NEB, M0253) was used to synthesize cDNA. 2X Realtime PCR Mix (Mei5 Biotech, MF013) and Applied Biosystems SteponePlus Real-Time PCR System (ThermoFisher) were used to quantify the cDNA in duplicate or triplicate for miRNA qRT-PCR.

Northern blot

For Northern blot, small RNA was enriched by 5 M NaCl and 30% PEG8000 (Sangon biotech, A600433) from total RNA for 1 h at 4°C. After centrifugation at 13,000 rpm for 45 min at 4°C, the supernatant was precipitated by 100% ethanol. Denatured small RNA (2 μg) was separated on a 15% Urea PAGE gel and transferred to Hybond N+ (Amersham Biosciences, RPN1210B) membranes by semi-dry transfer for 90 min at constant 10V. For detection of miRNA, membrane was chemically crosslinked with EDC (Sigma, E7750) for 2 h at 60°C. Indicated miRNA probes were 5'-labelled by T4 Polynucleotide Kinase (NEB, M0201L) and γ-^{32}P-ATP for 1 h at 37°C. Chemically-crosslinked membranes were hybridized with 5'-labelled miRNA probes in PerfectHyb™ Plus hybridization buffer (Sigma, H7033) overnight at 42°C. After hybridization, membranes were washed once with 2 × SSC and 0.1% SDS at 42°C for 10 min and twice with 1 × SSC and 0.1% SDS for 10 min at 42°C. Membranes were exposed to an imaging plate overnight and scanned using a laser scanner.

Luciferase reporter assay

The 3' untranslated regions (UTRs) of human *CCNE1* (1583 bp to 1942 bp), *CDK6* (7556 bp to 8155 bp), and *CDC25A* (2486 bp to 2873 bp) containing RDR1-targeted miRNA sites were PCR amplified and cloned into the XhoI and NotI sites of psiCHECK2 vector (Promega, C8021). As a control, the RDR1-targeted miRNA sites in the human *CCNE1*, *CDK6* UTRs were mutated using Q5 Site-Directed Mutagenesis Kit. For transfection, different cell lines were seeded in 6-well plates in the presence or absence of Dox (4 μg/ml) to induce RDR1 or RDR-Mut expression. After 96 h, the cells were transfected with 2 μg luciferase reporter plasmids using Lipofectamine™ 3000. The cells were harvested 48 h after transfection. The relative luciferase activity was measure by *TransDetect*® Double-Luciferase Reporter Assay Kit (Transgen, FR201) following the manufacturer's instructions.

siRNA knockdown

For DROSHA, DGCR8 and AGO2 knockdown, siRNAs and Lipofectamine 3000 reagent were diluted with Opti-MEM medium and incubated at room temperature for 15 min. Next, the mixtures were added to the 12-well plates seeded with 10,000 cells in advance. After 8 h of transfection, the medium was changed to normal culture medium with or without Dox (4 μg/ml). After 72 h, the cells were harvested and lysed for Western blot to verify the knockdown. After 120 h, the cells were counted using Coulter Counter and lysed for Western blot to detect the expression of different cell cycle proteins.

For AGO2 knockdown in RDR1 cell lines followed small RNA-seq assay, AtRDR1 expression was first induced in A549 cells with 4 μg/ml Dox for 48 h. Next, si*NC* and si*AGO2* were transfected into A549 cells as described above. After 48 h of transfection and Dox treatment, cells were harvested for Western blot analysis and small RNA-seq following the manufacturer's instructions.

Electrophoretic mobility shift assay

Chemically synthesized single-stranded miRNAs were heated to 94°C in duplex buffer (10 mM Tris-HCl [pH 7.6], 10 mM $MgCl_2$, 10 mM dithiothreitol) for 1 min and then gradually cooled. After annealing, the miRNA duplex was labelled with T4 PNK and γ-^{32}P-ATP at 37°C for 1 h. Subsequently, 50 nM of 5' labelled-miRNA duplexes were incubated with a dilution series of recombinant AGO2 proteins and recombinant RNasin® Ribonuclease Inhibitor in reaction buffer (20 mM Tri-HCl [pH 7.6], 67 mM NaCl, 10 mM DTT) for 30 min at 37°C. The concentration gradient of rAGO2 ranges from 0.039 to 1.25 μM. The mixture was analyzed by 5% Native PAGE on ice at 100V for about 2 h. Gels were exposed onto an imaging plate for 4 h and scanned using a laser scanner. The gray value of each band was measured by ImageJ. The fraction bound and Kd values were calculated by Prism 7.

For electrophoretic mobility shift assays of the binding of rAGO2 to 1nt-overhang miR-10a incubated with rAtRDR1 or rAtRDR1-Mut, 5′-PNK-labelled 1nt-overhang miR-10a was first incubated with rAtRDR1 or rAtRDR1-Mut and non-radioactive ATP, then purified and incubated with different concentrations of rAGO2 same above. The probe incubated with rAtRDR1 or rAtRDR1-Mut only was used as a negative control. Fraction bound was calculated by ImageJ and Kd values were obtained using Prism.

Microscale thermophoresis assay

Chemically synthesized FAM-labelled miRNAs were annealed at 94°C in duplex buffer for 1 min and then gradually cooled. After annealing, 100 nM of FAM-labelled miRNA duplexes were incubated with a dilution series of rAGO2 for 30 min at 37°C. The concentration gradient of rAGO2 ranges from 0.039 to 5 μM. The reaction mixture was then loaded into standard glass capillaries for MST assay. The MST assay was measured at room temperature using 20% LED power and 40% MST power in the MST machine (NanoTemper Technologies; München, Germany). Data were analyzed using the software MO.AffinityAnalysis and Prism 7.

Recombinant proteins expression and purification

The RNA-dependent RNA polymerase domain of *Arabidopsis thaliana* RDR1 spanning residues 372-931 (recombinant AtRDR1, rAtRDR1) was amplified by PCR and cloned into SalI and NotI sites of pETDuet-1 vector with a His_6-tag for protein purification. The catalytic center of AtRDR1 was mutated (recombinant AtRDR1-Mut, rAtRDR1-Mut) using the Q5 Site-Directed Mutagenesis Kit. Recombinant AtRDR1 and AtRDR1-Mut were expressed in Escherichia coli Transetta (DE3) cells (Transgen, CD801). Bacteria were cultured in LB media supplemented with 50 μg/ml ampicillin (Sangon biotech, B541011) and 25 μg/ml chloramphenicol (Sangon biotech, B541015). In addition, 1 mM Isopropyl β-D-Thiogalactoside (Sangon biotech, B541007) was added to induce rAtRDR1 and rAtRDR1-Mut expression. The bacteria were cultured at 16°C for 18 h. Bacteria were collected and washed with PBS. The pellets were resuspended with lysis buffer (20 mM Tris-HCl [pH 7.6], 150 mM NaCl, 1.5 mM $MgCl_2$, 10 mM imidazole, 1 mM Dithiothreitol (DTT) and 1 mM PMSF) and lysed using a high-pressure homogenizer. Following centrifugation at 17,000 g at 4°C for 45 min, the supernatant was incubated with IDA-Ni Beads (Beaverbio, 70501-5) at 4°C for 2 h. Next, the beads were washed twice with wash buffer (20 mM Tris-HCl [pH 7.6], 150 mM NaCl, 1 mM DTT) containing 80 mM imidazole (Sigma, I2399), resuspended in elution buffer (50 mM Tris-HCl [pH 7.6], 150 mM NaCl, 400 mM imidazole, 1 mM DTT) and then incubated at 4°C for 30 min to elute rAtRDR1 or catalytic mutant rAtRDR1-Mut.

His-tagged recombinant human AGO2 protein (>95% purity) was purchased from Sino Biological. Briefly, total human rAGO2 was (Met 1-Ala 859) was expressed with a polyhistidine tag at the N-terminus and affinity purified from baculovirus-insect cells.

In vitro RNA-dependent RNA polymerase assay

For *in vitro* RDR polymerase assay of miRNA duplexes with different overhang types, chemically synthesized single-stranded miRNAs were heated to 94°C in duplex buffer (10 mM Tris-HCl [pH 7.6], 10 mM $MgCl_2$, 10 mM dithiothreitol) for 1 min, gradually cooled and used as template for *in vitro* RNA-dependent RNA Polymerase Assay. Two microliters of rAtRDR1 or rAtRDR1-Mut (4 μg) were assayed in a 20 μl reaction mixture containing 50 mM Tris-HCl [pH 7.6], 8 mM $MgCl_2$, 0.1 mM EDTA, 1 μl RNasin (Promega, N2111), 0.25 μl α-^{32}P-ATP or GTP (~3,000 Ci per mmol) and 2 μl of 1 μM template RNA at 37°C. In addition, template RNA was labelled by γ-^{32}P-ATP with T4 PNK as control. For urea PAGE, the reaction product was mixed with 2X RNA Loading Dye (NEB, B0363S) and incubated for 5 min at 95°C. To separate the reaction products, 15% TBE-Urea Polyacrylamide gel was used. The gel was exposed onto an imaging plate for 2 h and scanned using a laser scanner. For double tailing assay, the first reaction product is purified by RNA Clean & Concentrator column (Zymo, R1017). The second reaction was performed essentially as the first reaction, except that non-radioactive ATP/GTP was used.

In vitro RNA-dependent RNA polymerase and AGO2 assay

For *in vitro* RDR1 and AGO2 coupling assay, chemically synthesized single-stranded miR-10a were annealed at 94°C in duplex buffer for 1 min and then gradually cooled (miR-10a with 2nt-overhang). One microliter of rAtRDR1 (2 μg) were assayed in a 10 μl reaction mixture containing 50 mM Tris-HCl [pH 7.6], 8 mM $MgCl_2$, 0.1 mM EDTA, 0.5 μl RNasin (Promega, N2111), 0.2 μl α-^{32}P-ATP (~3,000 Ci per mmol), 1 μl of 1 μM template RNA and rAGO2 with different concentration gradients for 30 min at 37°C. In addition, template RNAs were labelled by γ-^{32}P-ATP with T4 PNK as control. For urea PAGE, 15% TBE-Urea Polyacrylamide gel was used to separate the denatured reaction products. The gel was exposed to an imaging plate for 2 h and scanned using a laser scanner.

For *in vitro* RDR1 assay of free miRNA duplex, annealed miR-10a with 1nt- or 2nt-overhang was incubated with rAGO2 with different concentration gradients for 30 min at 37°C. rAtRDR1 and α-^{32}P-ATP were then immediately added to the reaction. The *in vitro* RNA-dependent RNA polymerase assay was performed essentially as described above. The 5′-PNK-labelled miRNAs were used as size markers. Annealed miR-10a incubated with rAtRDR1 only was used as a negative control. The coupling efficiency was calculated as: (the gray value of each band) / (the gray value of the corresponding negative control). The gray value of each band was measured by ImageJ.

Adeno-associated virus (AAV) production

AAV-CAG-FLAG-OsRDR1 for OsRDR1 expression was generated from AAV-CAG-EGFP vector. FLAG-OsRDR1 was cloned between the BamHI and EcoRI restriction sites of AAV-CAG-EGFP vector. AAV viral particles were produced in HEK293T cells. Briefly, AAV-CAG-FLAG-OsRDR1 (70 μg for 10 × 15 cm dishes), Rep/Cap (2/9) plasmids (70 μg for 10 × 15 cm dishes), and helper plasmids (200 μg for 10 × 15 cm dishes) were transfected into HEK293T cells using polyethyleneimine (Sigma, 919012) according to the manufacturer's instructions. Cells were harvested at 60 h post-transfection. AAV-OsRDR1 and AAV-EGFP viral particles were purified using iodixanol gradient ultracentrifugation. AVV virus was titered by qPCR using 2X Realtime PCR Mix (Mei5 Biotech, MF013). AAV was delivered into mice by *in situ* injection.

In vivo tumor models

Before injection, different cell lines transduced with lentivirus expressing RDR1 or RDR1-Mut were induced by 4 μg/ml Dox for 2 days. Dox-containing (1 mg/ml) drinking water was provided to the mice to induce the RDR1 expression.

Xenograft models

A549 cells (n = 5 for wild-type A549 group; n = 4 for RDR1-Mut group; n = 3 for AtRDR1 group; n = 5 for OsRDR1 group; 2x10^6 cells per mouse) and PC-3 cells (wild- type, RDR1-Mut, OsRDR1; 2x10^6 cells per mouse; n = 5 for each group) were injected into NOD.Cg-*Prkdc*^{scid}*Il2rg*^{tm1Vst}/Vst (NPG) mice. H1299 cells (wild-type, RDR1-Mut, OsRDR1; 2x10^6 cells per mouse; n = 5 for each group) were injected into NOD.Cg-*Prkdc*^{scid}*Il2rg*^{tm1Sug}/JicCrl (NOG) mice. All cells were injected subcutaneously into the flank. For A549 xenografts, mice were injected with 200 μl of 15 mg/ml D-Luciferin (Beyotime, ST198) 15 min prior to imaging using the IVIS Spectrum In Vivo Imaging System (Caliper Life Sciences). Images were analyzed using Living Image 3.0 software (Caliper Life Sciences). Tumor volume was assessed by calipers, and the tumors were dissected when tumor volume in control mice reached >750 mm^3. The tumors were weighed and photographed. For miRNA qRT-PCR, polyA(+) RNA-seq and Western blot, each biological sample is derived from tumors of 1-3 mice.

Xenotransplantation models

Jurkat cells (wild-type, RDR1-Mut, AtRDR1; 2x10^6 cells per mouse; n = 5 for each group) and NALM6 cells (wild-type, RDR1-Mut, OsRDR1; 1x10^6 cells per mouse; n = 5 for each group) were injected into NOD.Cg-*Prkdc*^{scid}*Il2rg*^{tm1Vst}/Vst (NPG) mice. K562 cells (wild-type, RDR1-Mut, AtRDR1, OsRDR1; 2x10^6 cells per mouse; n = 5 for each group) were injected into NOD.Cg-*Prkdc*^{scid}*Il2rg*^{tm1Sug}/JicCrl (NOG) mice. All cells were injected into the lateral tail vein. Jurkat, K562 and NALM-6 engraftment was assessed in the peripheral blood using the Beckman CytoFLEX S device. Briefly, 100 μl peripheral blood was taken weekly and lysed by lysing buffer (BD Pharmingen, 555899) to detect the proportion of EGFP+ cells. Dying mice with severely quadriplegic limbs were euthanized to collect whole blood and EGFP+ cells were sorted by BD FACSAria™ III. For miRNA qRT-PCR and polyA(+) RNA-seq, each biological sample was a pool of sorted cells from 4–5 female mice.

AAV delivery

For *in vivo* AAV-mediated RDR1 delivery, A549 cells (wild-type; 1x10^6 cells per mouse; n = 5 for each group) were injected into the flank of NOD.Cg-*Prkdc*^{scid}*Il2rg*^{tm1Vst}/Vst (NPG) mice. When tumors reached the mean size of 100 mm^3, mice were randomly divided into 2 groups at day 26. An intratumoral injection of 4E^{11} viral genome copies of AAV-OsRDR1 virus or AAV-EGFP control virus was performed at day 26. Tumor volume was evaluated by calipers. The tumors were weighed and then frozen in liquid nitrogen. For miRNA qRT-PCR, polyA(+) RNA-seq and Western blot, each biological sample is derived from tumors of 2-3 mice.

In vitro nanoparticle-mediated RDR1 delivery

A549, HeLa, H1299, NIH/3T3, RPE-1 cells were seeded at 50% confluency in 6 cm dishes before RDR1 delivery. The rAtRDR1 or rAtRDR1-Mut (8 μg) were mixed with 0.8 μg R-phycoerythrin (R-PE) protein and diluted with 400 μl 20 mM Hepes in a microcentrifuge tube. The protein solutions were mixed with 16 μl of PULSin (Polyplus-transfection, PT-501-04) and incubated for 15 min at room temperature. Before transfection, the culture media were replaced by serum-free DMEM. After 12 h of incubation with transfection mix at 37°C, the culture media containing proteins were removed. After 24 h of transfection, cells were digested and R-PE positive

cells were sorted by BD FACSAria™ III. For miRNA qRT-PCR and polyA(+) RNA-seq, samples were harvested 8 h after sorting. For living cell counting, cells were digested 48 h after sorting and stained by 0.4% trypan blue staining solution.

RNA-seq

Different cells with RDR1 or RDR1-Mut expression were harvested after 2 or 3 days of 4 μg/ml Dox treatment and after 5 or 6 days of 4 μg/ml Dox treatment. Different solid tumor tissues were quickly frozen in liquid nitrogen and then the RNA was extracted using homogenizer and TRIzol for polyA(+) RNA-seq. For library construction, 1 μg total RNA, TruSeq Stranded mRNA Sample Prep Kits (Illumina, RS-122-2101), VAHTS Stranded mRNA-seq Library Prep Kits (Vazyme, NR602) and VAHTS Ribo-off Globin & rRNA Depletion Kit (Vazyme, N408) were used following the manufacturer's instructions. Library samples were analyzed by Illumina HiSeq X Ten sequencing system.

Small RNA-seq

Total RNA was extracted from different RDR1 cell lines with Dox treatment for 5 or 6 days and corresponding wild-type cells. Spike in RNAs from S2 cells are added to each sample in proportion to the number of cells. 30 μg total RNA was loaded into 15% TBE-Urea gel (Invitrogen, EC6885BOX) and 15-50 nt small RNAs were separated. NEBNext® Small RNA Library Prep Set for Illumina kit (NEB, E7580L) was used to construct small RNA libraries according to the manufacturer's instructions. Library samples were analyzed by Illumina HiSeq X Ten sequencing system.

AGO2 CLIP-seq

For AGO2 CLIP, A549 and HepG2 stable cell lines were induced by 4 μg/ml Dox for 6 days, washed twice with PBS and UV irradiated 3 times at 2000J/cm^2. Cell were lysed in cold lysis buffer (20 mM Tris-HCl [pH 7.6], 137 mM NaCl, 1 mM EDTA, 1% Triton X-100, 1.5 mM $MgCl_2$) supplemented with 1:200 Protease Inhibitor Cocktail (Sigma, P8849) and 1 U/μl RNasin® Ribonuclease Inhibitor (Promega, N2111) on ice for 30 min. After centrifugation at 14,000 rpm for 30 min at 4°C, cell lysates were subjected to protein A Dynabeads (Life Technologies, 10001D) coated with the monoclonal mouse anti-human Ago2 for 3 h at 4°C (clone 2E12-1C9, Abnova, H00027161-M01). Beads were then washed 3 times with PBS containing 0.02% Tween-20 (PBST). A small aliquot of beads was resuspended in 4 × NuPAGE™ LDS sample buffer for Western blot. The remaining beads were treated with 4 mg/ml proteinase K for 30 min at 50°C and subsequent phenol/chloroform extraction. CLIP-RNA libraries were constructed using the small RNA library and ribo-off RNA-seq preparation protocol as described above. All libraries were sequenced on Illumina HiSeq X Ten sequencing system.

miRNA transfection assay

For miR-34c transfection assay, HepG2-AtRDR1 stable cell line was induced by 4 μg/ml Dox for 3 days. Annealed miR-34c (2nt- or 1nt-overhang) and single-stranded miR-34c-5p (1nt-shorter) were transfected by Lipofectamine 3000 (30 μl of 1 μM template RNA for each 15 cm plate). After 48 h of transfection, cells were harvested for AGO2 CLIP-seq.

Single-cell RNA sequencing

For single-cell RNA sequencing of Jurkat xenograft, Jurkat cells (vector, AtRDR1; 1.5x10^6 cells per mouse) were injected into the lateral tail vein of NOD.Cg-*Prkdc*^{scid}*Il2rg*^{tm1Sug}/JicCrl (NOG) mice. Dox-containing (1 mg/ml) water was administered orally to induce the AtRDR1 expression in Jurkat xenograft model. Jurkat engraftment was assessed weekly using the Beckman CytoFLEX S device. After 34 and 36 days, mice of the vector group and the AtRDR1 group were euthanized respectively and EGFP+ cells were sorted by BD FACSAria™ III. EGFP+ cells were resuspended in 1X PBS containing 0.04% BSA and washed twice. Then, the concentration of cell suspensions was adjusted to 900-1200 cells/μl. In total, 16,000 living cells were loaded and libraries were constructed using Chromium Next GEM Single Cell 3' Kit v3.1 (10x Genomics, 1000268) according to the manufacturer's instructions. Purified libraries were analyzed by Nova-seq 6000 sequencing system.

PolyA(+) RNA-seq analysis

To analyze polyA(+) RNA-seq data, adapters of raw data were trimmed with Trimmomatic software. The quality of these data was evaluated by FastQC software. HISAT2 software with default parameters was used to align sequences to the human genome (hg38, UCSC) and the mouse genome (mm10, UCSC) based on the origin of the cell lines. Output files after sequence alignment were used to obtain gene count matrix with featureCounts software using corresponding UCSC RefSeq as gene annotations. For further analyses, gene counts in each sample were normalized to the total reads of the library to calculate reads per million (RPM). To compare gene expression levels between two samples, fold change (FC) of a gene was calculated using the following formula: (RPM of sample A+1) / (RPM of sample B+1). Relative value is calculated using this formula: (value in sample A)/(value in sample A + value in sample B).

Gene set enrichment analysis

Gene Set Enrichment Analysis (GSEA) software was used to perform enrichment analysis for genes. Maximum size of gene set was set at 1000. Gene sets used in GSEA, including KEGG, REACTOME and GO Biological Process, were obtained from

MSigDB (v7.4, http://www.gsea-msigdb.org/gsea/msigdb/). Cell cycle genes were obtained from KEGG_CELL_CYCLE and REACTOME_CELL_CYCLE_MITOTIC gene sets in MSigDB. Gene Ontology (GO) analysis was performed with ToppFun tool of ToppGene Suite (https://toppgene.cchmc.org/), using Biological Processes of GO as dataset.

Prediction of miRNA targets and CDF plots of target genes

The predicted miRNA targets were downloaded from TargetScan (Release 7.1, http://www.targetscan.org/vert_71/), using default predictions. The miRNA target network was made using Cytoscape software. Cumulative distribution function plot (CDF plot) was used to show the difference of numerical distribution. In order to identify the miRNA target genes enriched in each group (groups with and without RDR1 expression, IP group and input group), RNA-seq data and small RNA-seq data were combined in this analysis. Specifically, miRNAs with both high expression (top-10 highest expressed miRNAs) and differential expression (fold change>1.25) after RDR1 expression were used in target gene prediction with TargetScan. After filtering low expression genes (RPM<5 in all samples), total genes were grouped into targeted genes and non-targeted genes according to whether they were predicted in the previous step. Fold change (FC) of gene expression was calculated by (gene expression with RDR1 expression + 1) / (gene expression without RDR1 expression + 1) or (gene expression in AGO2-IP group + 1) / (gene expression in input group + 1).

Processing of small RNA-seq data and annotation of small RNAs

Perl and python scripts were used to analyze small RNA-seq data. Adapters of sequences were trimmed and sequences with a length of 19-25nt were retained. In order to identify the class of small RNA sequences (rRNA, tRNA, miRNA, snoRNA, snRNA, lncRNA, mRNA and repeat sequences), Bowtie software was used to align them to the reference sequences without mismatch. The reference sequences were downloaded from the following databases: rRNA, snRNA and snoRNA and mitochondrial genome from NCBI (https://www.ncbi.nlm.nih.gov/), miRNA from miRbase (http://www.mirbase.org/), tRNA from GtRNAdb (http://gtrnadb.ucsc.edu/), lncRNA and mRNA from (https://www.gencodegenes.org/), repeat sequence from RepeatMasker reference from UCSC browser (http://genome.ucsc.edu/cgi-bin/hgTables). 30nt upstream and 30nt downstream of tRNA references were added referring to genome. If a sequence could be annotated more than one type of small RNA, we prioritized the classes as follows: rRNA, tRNA, miRNA, snoRNA, snRNA, lncRNA, mRNA, repeat sequences and mitochondrial genome. Sequences without annotation were annotated as unknown.

Alignment of miRNAs

To build the index of miRNA, we downloaded the mature miRNA sequences from miRBase, 3nt upstream and 3nt downstream of mature miRNA were added to the references. Each sequence was aligned to the reference using Bowtie software using the following parameters: -a -v 1 -3 3.

Annotation for sequences aligned to miRNA reference

To make detailed annotation for aligned sequences, we first defined ‘‘tail’’ and ‘‘mismatch’’ of this analysis. For each sequence, one or more consecutive bases at the 3’ end which did not match miRNA reference were defined as ‘‘tail’’, and other bases which did not align to reference were defined as ‘‘mismatch’’. Only the sequences with 0-1nt mismatch and 0-3nt tail were used for further analysis.

When sequences were aligned to more than one mature miRNA, the best alignment was selected for analysis. The best alignment was firstly defined as the one with the least number of mismatches and secondly with the shortest tail. If the number of mismatches and the length of tail were both the same in two or more alignments, these alignments were all considered as best alignments for this sequence. For each mature miRNA, we chose the most abundant sequence without mismatch and tail in WT or (-)Dox sample.

Normalization of miRNA data

In order to compare the miRNA expression in the line, the count of miRNAs was normalized.

In RDR1 expression group, two ways were used to normalize miRNA data. Fly miRNA was added as spike-in in some samples. In non-spike-in method (including A549, HeLa, HepG2, HCT116 and NIH/3T3), the numbers of miRNAs were normalized to the numbers of total reads of the corresponding library to calculate RPM. In spike-in method (including H1299, Jurkat and RPE-1), the number of miRNAs was multiplied by a factor to make the count of fly miRNAs equal in all samples in a cell line. We used the top-10 highest expressed miRNAs as reference, which did not contain identical miRNAs in fly and human/mouse. Each of these 10 miRNAs was used to calculate a factor and the mean of these 10 factors was used as the factor for this sample for normalization. After normalization between samples within cell lines, the normalized reads of the sample with higher miRNA expression level was set at one million.

In cell cycle inhibition, AGO2-CLIP and AGO2 knockdown experiments, miRNA expression was normalized with non-spike-in method. Some cell lines of RDR1 expression group were used in this analysis (A549, HeLa, HepG2). In order to be consistent with the previous analysis in RDR1 expression group, the normalized reads of the sample with higher miRNA expression level of RDR1 expression group was set at one million.

In the miR-34c transfection assay, miRNA expression was normalized to the expression of endogenous miRNA, which was set at one million. In IP(-)Dox and IP(+)Dox group, relative abundance was calculated by (expression of transfected miR-34c in samples with 1nt-overhang) / (expression of transfected miR-34c in samples with 2nt-overhang).

Tailing analysis and end type analysis of small RNA-seq data

For tailing analysis, tailing percentage means the percentage of non-template mononucleotide-tailed sequence of each miRNA. In order to detect the overhang of miRNA, stem-loop sequence of miRNAs was obtained from miRBase and the annotation of overhang on each mature miRNA was determined. For every overhang analysis, only miRNAs with 2nt-overhang as the main overhang type were used, which account for the majority of the total miRNAs.

Analysis of miRNA isoform for TCGA patient samples and published data

miRNA isoform data of The Cancer Genome Atlas (TCGA) were available from Genomic Data Commons Data Portal (GDC, https://portal.gdc.cancer.gov/) and all ''Isoform Expression Quantification'' files for TCGA patients available were downloaded using the GDC Data Transfer Tool. Other published data were available from Gene Expression Omnibus (GEO, https://www.ncbi.nlm.nih.gov/geo/) and analysis methods followed the methods mentioned previously. Please check Table S4 for the information.

In the comparation of cancer samples (TCGA patients, non-TCGA patients and cancer cell lines) and normal samples, miRNAs with low expression (median of cancer samples<100 or median of normal samples<100) aren't included in further analyses. The relative ratio is calculated using the formula: (RPM of 1nt-shorter miRNA +10) / (RPM of 1nt-shorter miRNA + RPM of 2nt-overhang miRNA + 20).

Single-cell RNA-seq data analysis

To analyze scRNA-seq data, cellranger software was used to align sequences to reference genome and gene count matrix was generated using ''count'' command. hg38 genome and mm10 genome were merged as the reference. Seurat R package was used to merge the scRNA-seq samples. We used the following filtration criteria for the merged sample: nFeature > 500, percentage of hg38 mitochondria genes < 20%, and percentage of sequence aligned to hg38 > 90%. ''LogNormalize'' function was used to normalize the count matrix. For principal component analysis (PCA), 2000 variable genes were used using ''runPCA'' function. ''FindNeighbors'' and ''FindClusters'' functions were used to find shared nearest neighbors and identify clusters. UMAP dimensionality reduction was generated with ''RunUMAP'' function. Cell cycle score was calculated using the function ''CellCycleScoring''.

QUANTIFICATION AND STATISTICAL ANALYSIS

The statistical details and methods are indicated in the figure legends or methods. Statistical analysis was performed by GraphPad Prism 7 and R software version 3.5.1. Data were presented as mean ± SEM or mean ± SD with at least three technical replicates unless otherwise indicated. Statistical results were considered significant when $p < 0.05$. The statistical tests used and the p-values are listed in the figures and figure legends.

CellPress

Supplemental figures

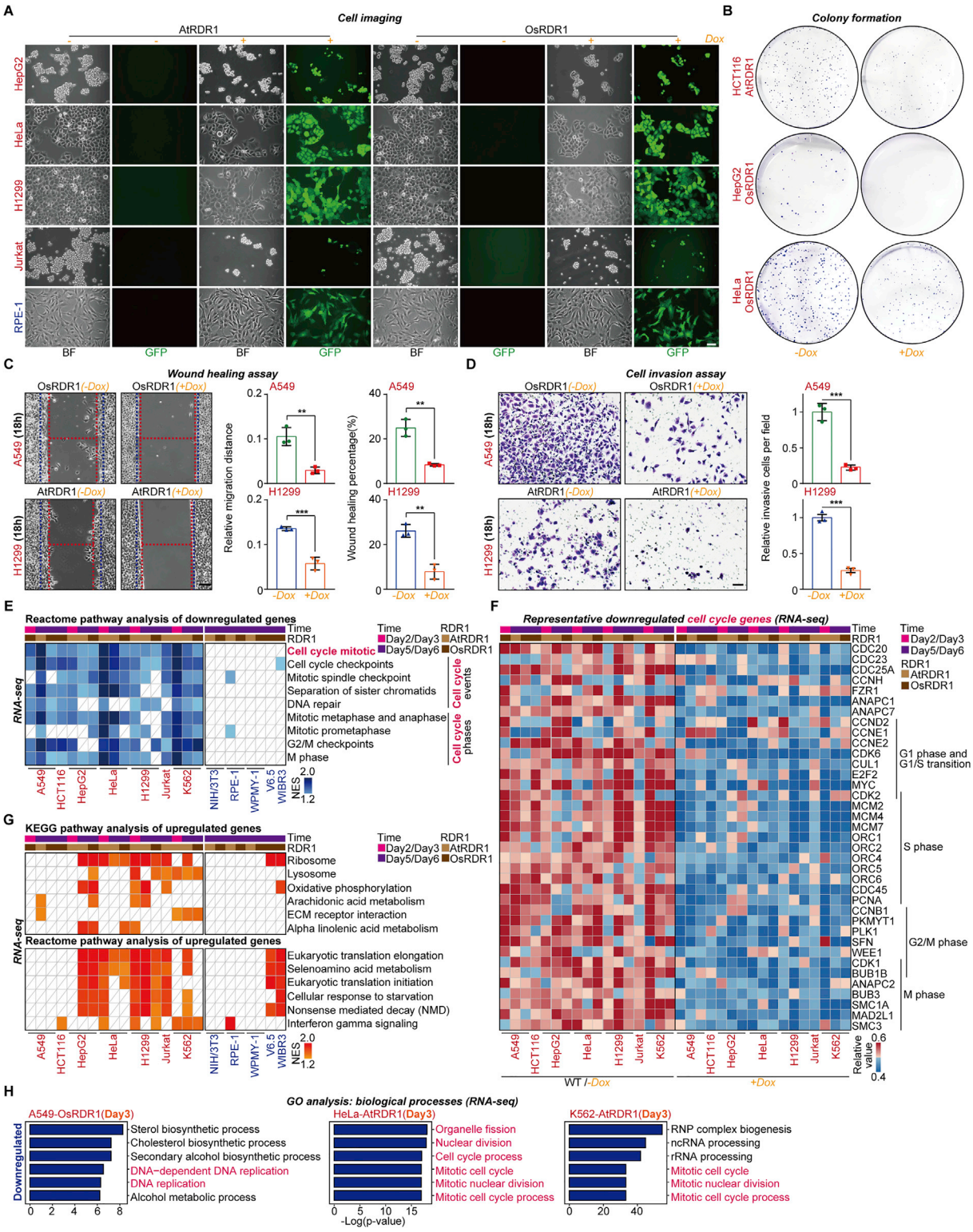

(legend on next page)

Figure S1. Ectopic expression of plant immune protein RDR1 broadly represses cancer cell proliferation by interfering with cell-cycle process, but does not affect non-cancer cells, related to Figure 1

(A) Representative images of indicated RDR1-stable cell lines with co-expression of EGFP induced by 4 μg/mL Dox for 60 h BF, bright field. Scale bars, 100 μm.

(B) Representative images of colonies of HCT116, HepG2, and HeLa cells with AtRDR1 or OsRDR1 expression for 7 days (n = 3).

(C) Representative images (left panel) and quantification (right panel) of relative migration distance and wound-healing percentage of A549 and H1299 cells at 18 h time point after RDR1 expression for 4 days (n = 3). Quantifications of relative migration distance and wound-healing percentage were performed by ImageJ (Fiji). Scale bars, 100 μm.

(D) Representative images (left panel) and quantification (right panel) of invasive A549 and H1299 cells at 18 h time point after Dox induction for 3 days (n = 3). Scale bars, 100 μm.

(E) Significantly downregulated pathways in GSEA analysis for Reactome gene sets. Pathways are downregulated in RDR1 expression group, compared with wild-type and (−)Dox groups. Pathways with p value less than 0.05 are considered significant and colored with blue, according to the normalized enrichment score (NES). Number of days after RDR1 expression are indicated with pink (day 2 or day 3) and purple (day 5 or day 6).

(F) Heatmap of the relative value of representative downregulated cell-cycle genes. Relative value is calculated by dividing gene expression by the sum of the gene expression in wild-type or (−)Dox and RDR1 expression groups. Left: wild-type and (−)Dox groups; right: RDR1 expression groups. Number of days after RDR1 expression are colored with pink (day 2 or day 3) and purple (day 5 or day 6).

(G) Significantly upregulated pathways in GSEA analysis, according to the schematic illustration in (E).

(H) GO analysis of RNA-seq data. Pathways are downregulated in RDR1 expression group, compared with wild-type and (−)Dox groups. Biological processes of gene ontology (GO) is used as dataset for analysis.

Data are presented as mean ± SD (C and D). $^{**}p < 0.01$, $^{***}p < 0.001$ by unpaired Student's t test (C and D).

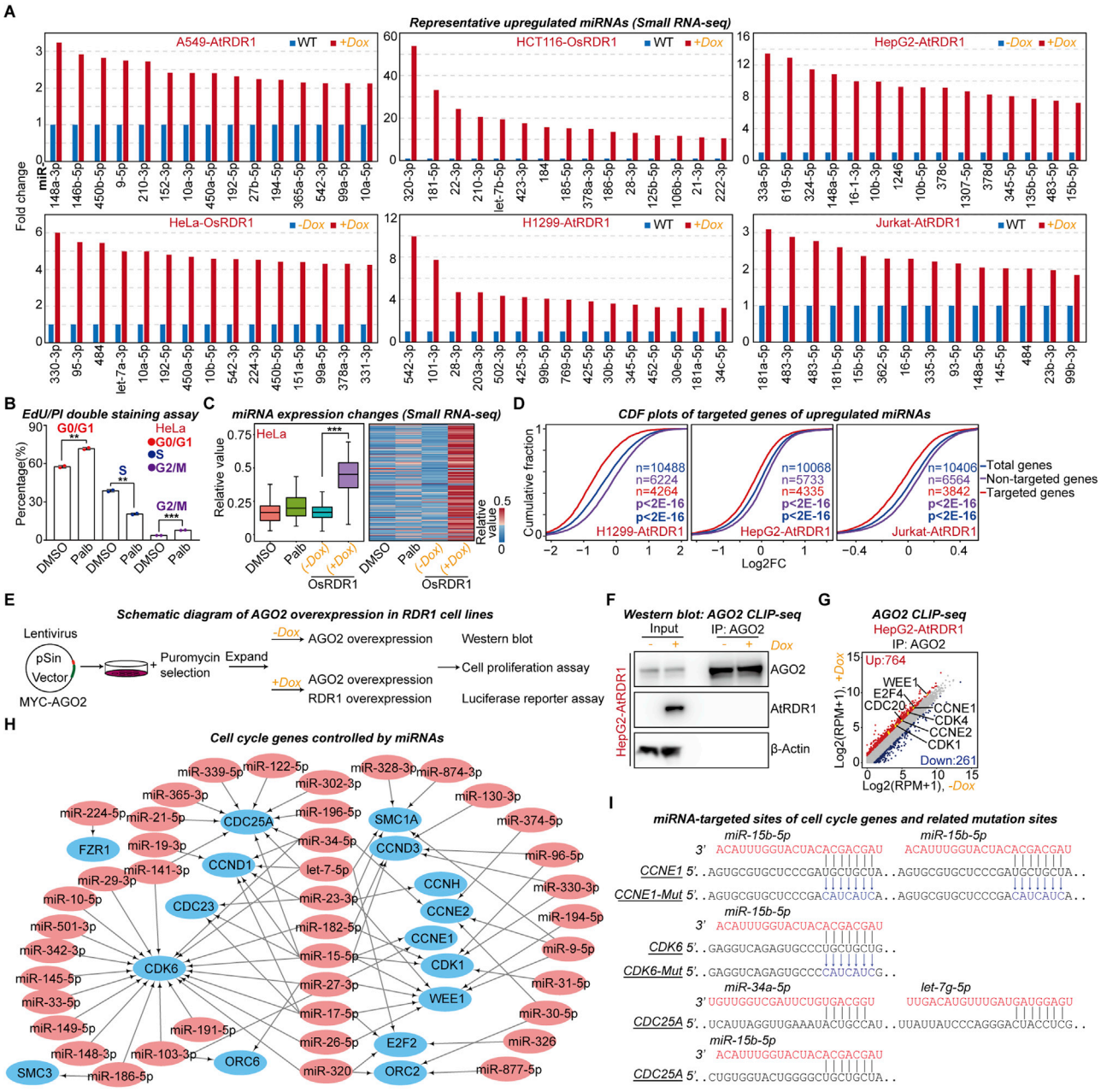

Figure S2. Plant RDR1 elevates miRNA expression, and miRNA pathway is indispensable for RDR1 antitumor functions, related to Figure 2

(A) Examples of upregulated miRNAs. Fold change, compared with wild-type or (−)Dox groups in each cell line.

(B) Quantification of percentages of different cell-cycle phases in HeLa cells treated with 0.5 μM palbociclib or DMSO for 48 h (n = 2).

(C) miRNA expression changes after cell-cycle inhibitor treatment and RDR1 expression. Relative value of miRNA expression is normalized to the sum of miRNA expressions in all four samples.

(D) CDF plots of indicated cancer cell lines with RDR1 expression. FC, fold change, is calculated by dividing the normalized reads in (+)Dox group by wild-type group and (−)Dox group. miRNAs with both high expression (top 10 highest expressed miRNAs) and differential expression (FC > 1.25) are used in prediction. Targeted genes are predicted by TargetScan as described in methods. For total genes and non-target genes, p value is relative to targeted genes.

(E) Schematic representation of AGO2 overexpression in RDR1-stable cell lines to detect the effect on cell proliferation, target gene repression, and cell-cycle protein expression.

(F) AGO2 immunoprecipitation (IP) from HepG2 cells with AtRDR1 expression.

(G) Dot plot of gene expression in AGO2 CLIP-seq data. Representative cell-cycle genes are colored with yellow. Upregulated genes (FC > 1.5) are marked red, and downregulated genes (FC < 0.67) are marked blue.

(H) Network of miRNAs and cell-cycle genes. Arrow represents the miRNA-target gene relationship, predicted by TargetScan.

(legend continued on next page)

(I) miRNA target sites on *CCNE1*, *CDK6*, and *CDC25A* mRNAs. Point mutations introduced into the seed sequences on *CCNE1* and *CDK6*, and the mutation sequences are shown in blue.

Data are presented as mean ± SD (B). $^{**}p < 0.01$, $^{***}p < 0.001$ by unpaired Student's t test (B), two-sided Wilcoxon rank-sum test (C), and two-sided Kolmogorov-Smirnov test (D).

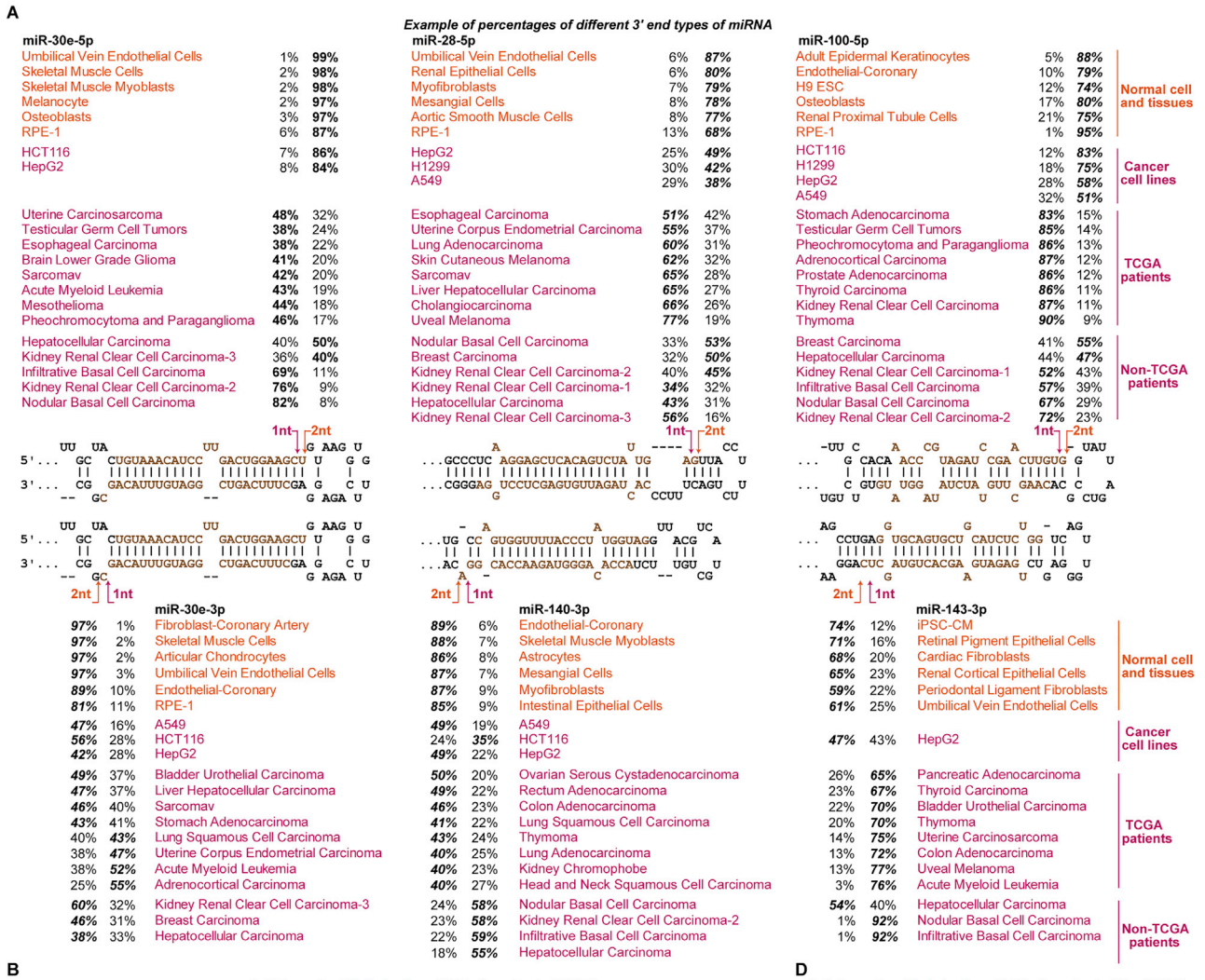

(legend on next page)

Figure S3. Abnormal 1-nt-shorter miRNA isoforms are widely accumulated in different human tumors, and RDR1 modifies these problematic miRNAs by mononucleotide tailing, related to Figure 3

(A) 3′ end types of selected mature miRNAs are shown in stem-loop structures. Arrows show end positions of mature miRNAs, with numbers indicating frequencies of these sites. Proportions are relative to untailed miRNAs. Mature miRNAs with 2 nt overhang are shown in brown. "1 nt" and "2 nt" represent the type of overhang.

(B) The relative ratio of 1-nt-shorter miRNA isoforms from TCGA patients is shown in boxplots. The ratio is calculated using this formula: (RPM of 1-nt-shorter miRNA + 10)/(RPM of 1-nt-shorter miRNA + RPM of 2-nt-overhang miRNA + 20). For each miRNA, the median of ratio in all patients represents the ratio in each cancer type. In this panel, 32 cancer types are shown.

(C) Percentage of miRNAs with higher relative ratio of 1-nt-shorter miRNA isoforms in each cancer type of TCGA. The ratio is calculated as described in (B). Compared with normal tissue, for each miRNA, if (the ratio in cancer-the ratio in normal tissue) > 0.15, this miRNA is defined as miRNA with higher relative ratio. Percentage of miRNAs with higher ratio is relative to the total number of comparable miRNAs with 2 nt overhang in normal tissue. The number shown on the right side of the panel means "number of miRNAs with higher relative ratio/number of miRNA used in this analysis."

(D) The relative ratio of 1-nt-shorter miRNA isoforms from non-TCGA patients is shown in heatmap. The ratio is calculated using the formula displayed in (B). Each row represents one mature miRNA, and each column represents a patient sample. *Z* score is used to normalize the overhang ratio for each miRNA. "BCC," basal cell carcinoma; "BRCA," breast invasive carcinoma; "KIRC," kidney renal clear cell carcinoma; "LIHC," liver hepatocellular carcinoma.

(E) Examples of miRNA duplexes with different end types are shown. Percentage is relative to total non-templated isoform of miRNAs. Brown, 2-nt-overhang miRNA duplexes in stem loop; orange, 2-nt-overhang miRNA sequences; purple, 1-nt-overhang miRNA sequences. Relative value is calculated using this formula: (value in sample A)/(value in sample A + value in sample B).

***$p < 0.001$ by two-sided Wilcoxon rank-sum test (B).

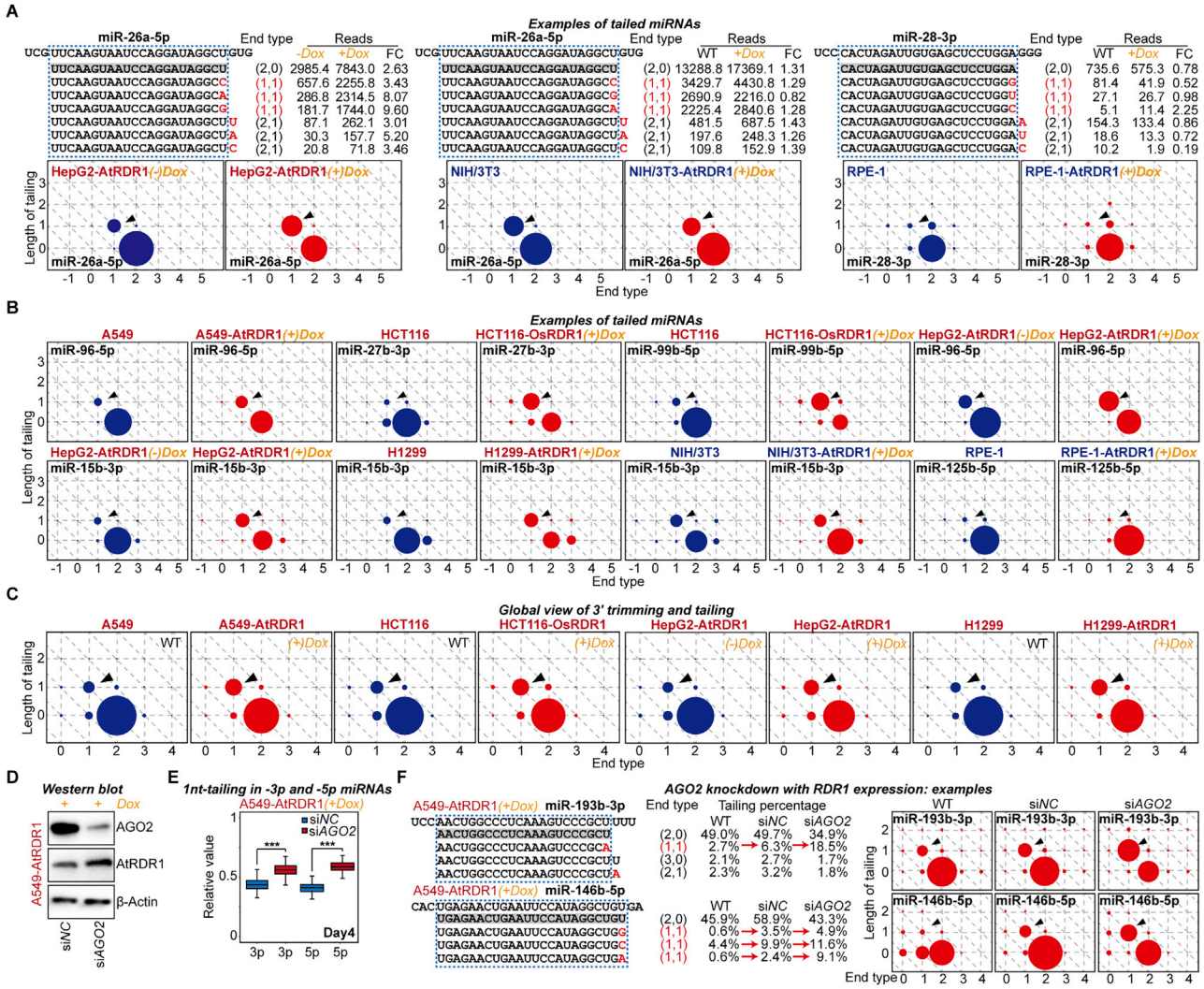

Figure S4. Abnormal 1-nt-shorter miRNA isoforms are widely accumulated in different human tumors, and RDR1 modifies these problematic miRNAs by mononucleotide tailing, related to Figure 3

(A) miRNA examples with corresponding reads and dot plot displaying the end type.

(B) Dot plots showing the end types of miRNA examples.

(C) Dot plots showing the end types of each group. The median of proportion for each miRNA in the group is shown. For (A), (B), and (C), end type is shown with a number pair: (overhang type, length of tailing). x axis of the dot plots represents the end position and y axis of the dot plots represents the length of tailing. The area of each dot is proportional to the percentage of reads of the mature miRNA.

(D) Western blot analysis of the AGO2 expression after siRNA transfection for 2 days.

(E) Tailing percentage of 1-nt-tailed miRNAs in -3p and -5p miRNAs. Relative value is calculated using this formula: (tailing percentage in sample A)/(tailing percentage in sample A + tailing percentage in sample B). "si," siRNA; "NC," negative control.

(F) Examples of miRNA sequences with different end types and tails are shown in tables and dot plots. Tails of each sequence are shown in red. Sequences in gray boxes are templated 2 nt overhang reads. End type is shown with an ordered pair: (overhang type, length of tailing). This ordered pair corresponds to the coordinates in dot plots. The area of each dot is proportional to the percentage of reads of the mature miRNA. Red arrows indicate an increase in tailing percentage.

***$p < 0.001$ by two-sided Wilcoxon rank-sum test (E).

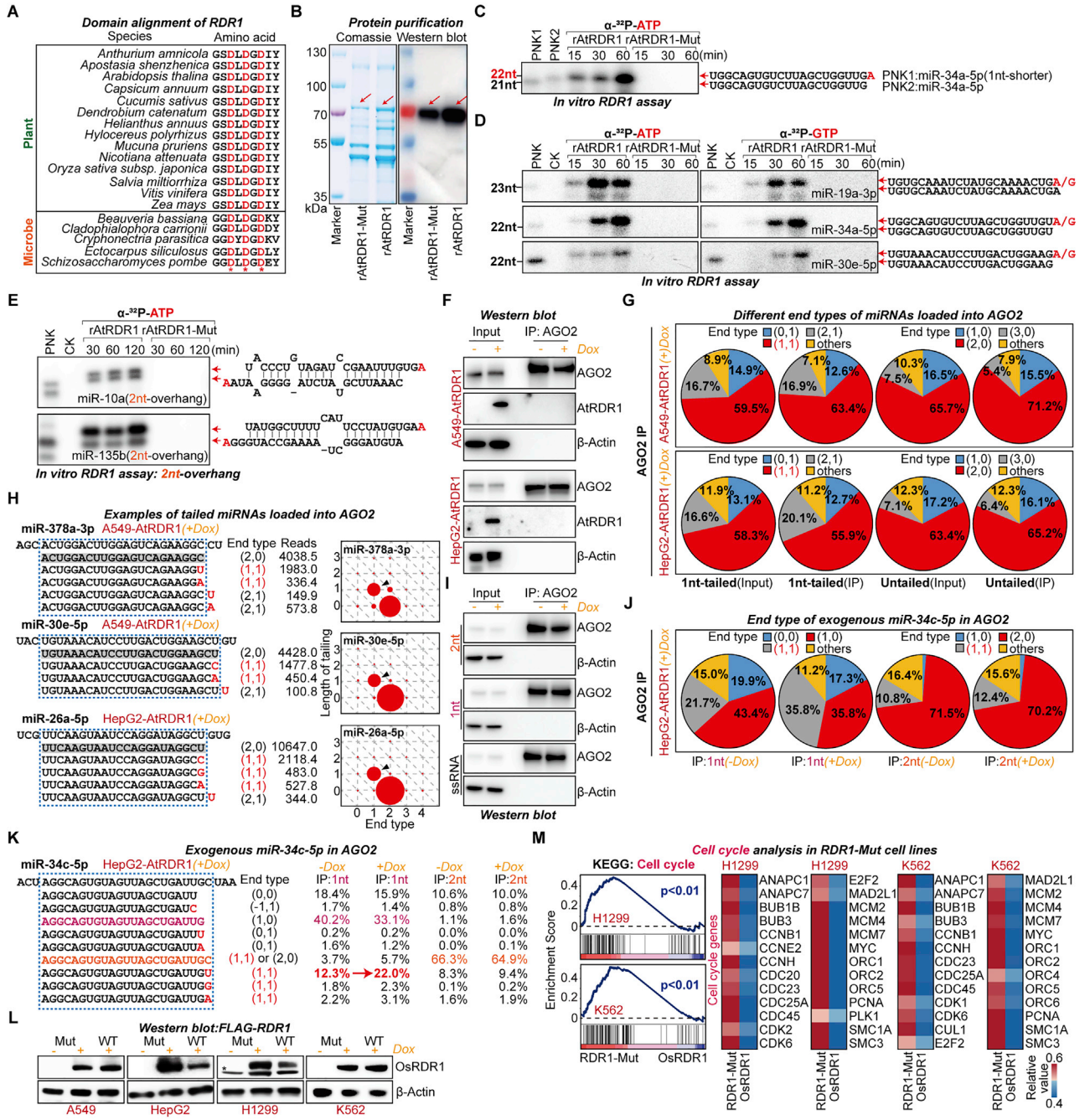

Figure S5. RDR1 can recognize and tail AGO2-dissociated miRNA duplexes with 1 nt overhang to restore their loading efficiency into AGO2 and stabilize miRNAs to rescue miRNA deficiency, related to Figure 4

(A) Comparison of conserved catalytic sites of RDR1 in plants and microbes.

(B) Purification of recombinant AtRDR1 and AtRDR1-Mut from *E. coli*. Left panel showing the staining of purified rAtRDR1 and rAtRDR1-Mut proteins. Right panel showing the western blot analysis of purified rAtRDR1 and rAtRDR1-Mut proteins with His_6-tag.

(C) *In vitro* RDR1 assay of rAtRDR1 or its mutant rAtRDR1-Mut, using chemically synthesized miRNA substrates (miR-34a-5p and 1-nt-shorter miR-34a-5p) in the presence of α-^{32}P-ATP. The 5′ PNK-labeled miRNAs were used as size markers.

(D) *In vitro* RDR1 assay of miRNAs with different lengths and strands, using rAtRDR1 or rAtRDR1-Mut. The experiments were performed essentially as in (C), except that in addition to α-^{32}P-ATP, α-^{32}P-GTP was used.

(E) *In vitro* RDR1 assay of rAtRDR1 or its mutant rAtRDR1-Mut, using annealed chemically synthesized miRNA substrates (miR-10a, -27a, and -135b) in the presence of α-^{32}P-ATP. The 5′ PNK-labeled miRNAs were used as size markers. The red arrows represent the tailed miRNA sequences with additional A.

(F) AGO2 immunoprecipitation (IP) from A549 and HepG2 cells with AtRDR1 expression.

(legend continued on next page)

(G) End types of miRNAs in AGO2-IP and input groups. Total value for calculating the proportion is the total 1-nt-tailed miRNA and untailed miRNA expression in the group. Mean in each group is shown with pie chart.
(H) Dot plots showing the end types of miRNA examples in AGO2-IP group. The median of proportion for each miRNA in the group is shown. End type is shown with a number pair: (overhang type, length of tailing). x axis of the dot plots represents the end position and y axis of the dot plots represents the length of tailing. The area of each dot is proportional to percentage of reads of the mature miRNA.
(I) AGO2 immunoprecipitation (IP) from HepG2 cells with AtRDR1 expression in miR-34c transfection assay.
(J) End types of miRNAs in AGO2-IP of HepG2-AtRDR1(+)Dox group in miR-34c transfection assay. Total value for calculating the proportion is the total 1-nt-tailed miRNA and untailed miRNA expression in the group. Mean in each group is shown with pie chart.
(K) miR-34c-5p sequences with different end types and tails are shown in tables. Tails of each sequence are shown in red. Sequence in purple is transfected 1-nt-overhang miR-34c, and sequence in orange is transfected 2-nt-overhang miR-34c. Red arrows indicate increases in tailing percentage.
(L) Western blot analysis comparing the expression levels of wild-type OsRDR1 and catalytic mutant RDR1-Mut in A549, HepG2, H1299, and K562 cells with 4 μg/mL Dox induction for 72 h.
(M) GSEA of RNA-seq data from cells of RDR1-Mut versus OsRDR1 group, using the cell-cycle gene set annotated in the KEGG (left panel). Heatmap of the relative expression of representative cell-cycle genes in RNA-seq data of RDR1-mut groups (right panel).

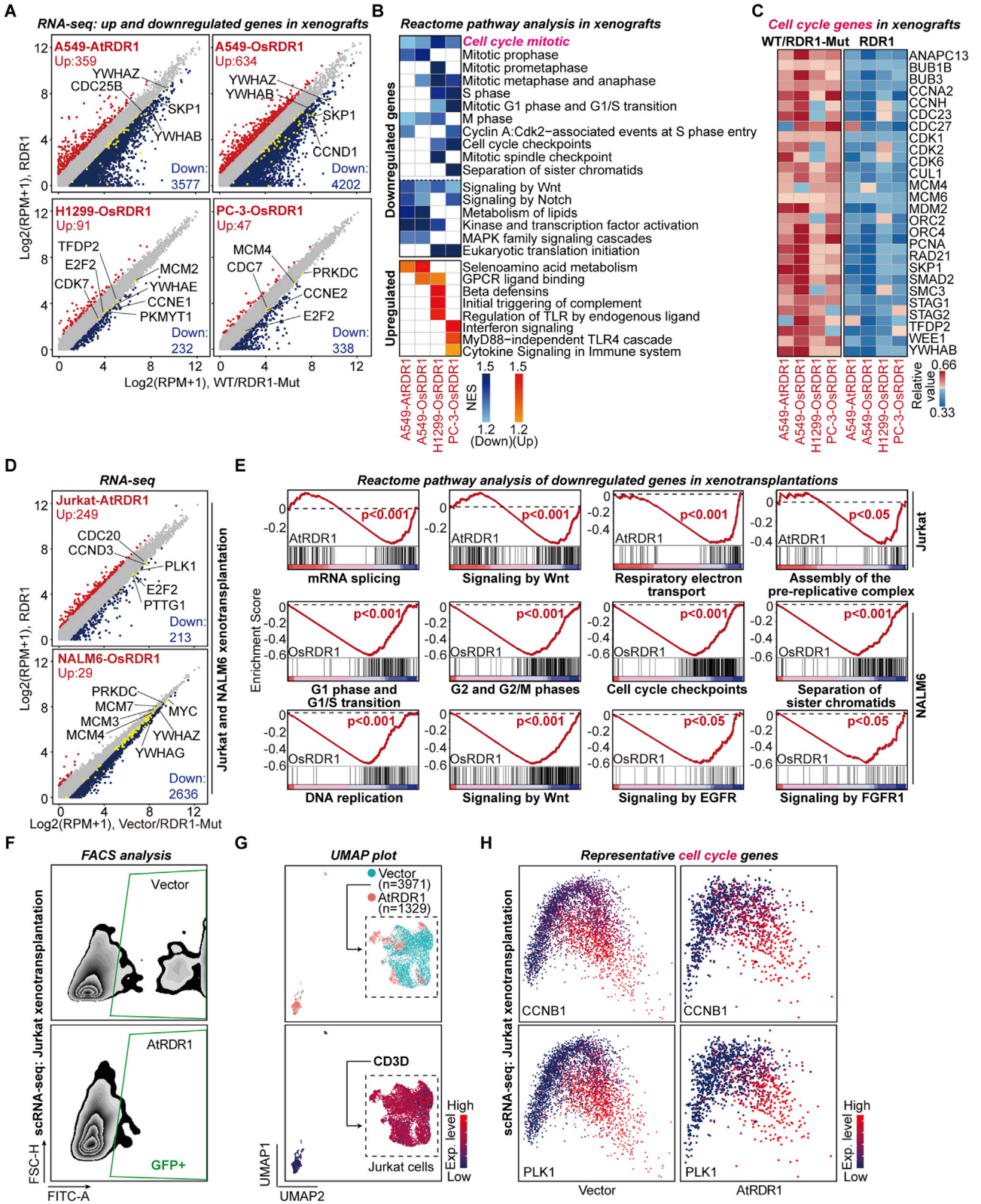

(legend on next page)

Figure S6. RDR1 suppresses solid tumor growth and inhibits leukemia proliferation in mice *in vivo*, related to Figures 5 and 6

(A) Scatterplot of gene expression in RNA-seq data of tumors with RDR1 expression from different xenograft models. Upregulated genes (FC > 2) are shown in red, and downregulated genes (FC < 0.5) are shown in blue. Representative RDR1-targeted cell-cycle genes are marked yellow.

(B) GSEA analysis of RNA-seq data from the tumors of wild-type, RDR1-Mut versus RDR1 group in different xenografts. Pathways with p value less than 0.05 are considered significant and are marked blue or red according to NES.

(C) Heatmap of the relative expression of commonly downregulated RDR1-targeted cell-cycle genes in different xenografts. Left: wild-type and RDR1-Mut groups; right: RDR1 expression groups.

(D) Scatterplot of gene expression in RNA-seq data of EGFP+ cells with RDR1 expression from Jurkat and NALM6 xenotransplantation models. Upregulated genes (FC > 2) are marked red, and downregulated genes (FC < 0.5) are marked blue. Downregulated RDR1-targeted cell-cycle genes are shown in yellow.

(E) Enrichment plot of GSEA analysis of downregulated genes in RNA-seq data from Jurkat and NALM6 xenotransplantation models. Pathways with p value less than 0.05 are considered significant. The left side of each plot represents RDR1 expression group, and the right side represents vector and RDR1-Mut groups.

(F) Flow cytometry analysis of EGFP+ cells used for scRNA-seq in Jurkat xenotransplantation model.

(G) UMAP plot of merged scRNA-seq data. Top: colored with sample source. Bottom: colored with relative expression level of *CD3D*.

(H) PCA plot of scRNA-seq data. The relative expression levels of two G2/M markers, *CCNB1* and *PLK1*, are shown in plot.

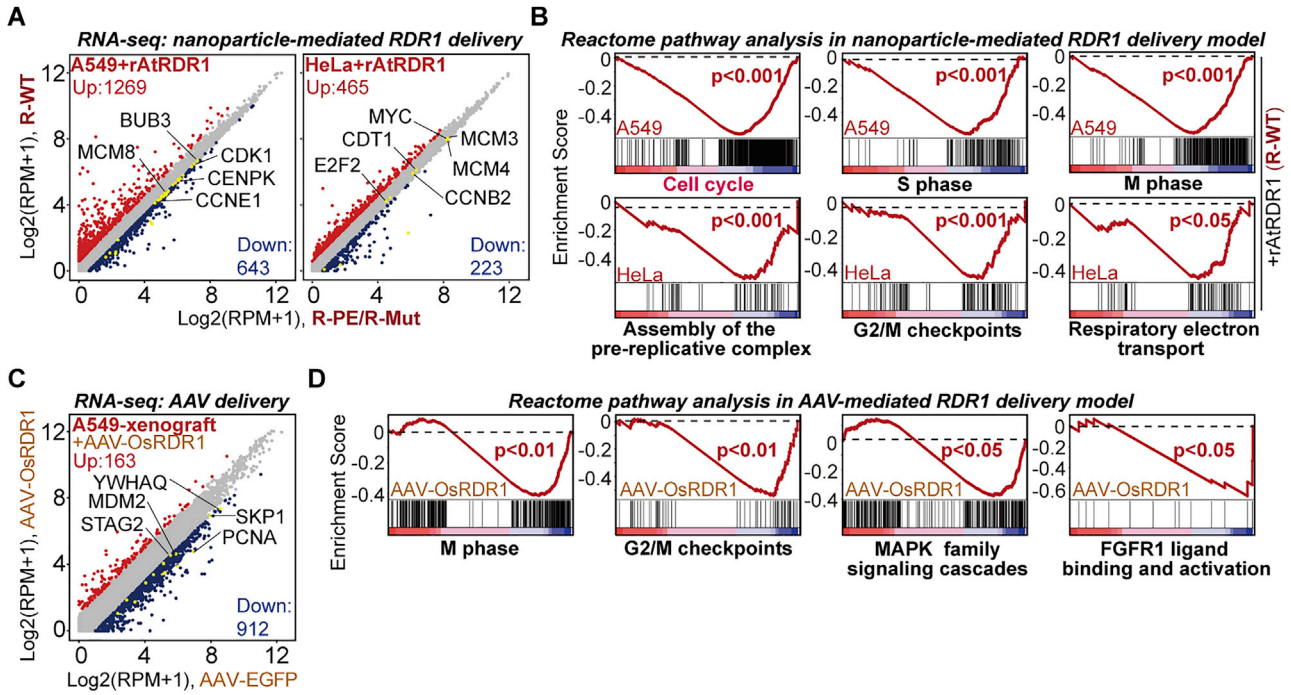

Figure S7. RDR1 delivered by nanoparticles and AAV can inhibit cancer cell proliferation *in vitro* and solid tumor growth in mice *in vivo*, respectively, related to Figure 7

(A) Scatterplot of gene expression in RNA-seq data of A549 and HeLa cells after nanoparticle-mediated RDR1 delivery. Upregulated genes (FC > 1.5) are marked red, and downregulated genes (FC < 0.67) are marked blue. Downregulated RDR1-targeted cell-cycle genes are shown in yellow.

(B) Enrichment plots of Reactome analysis of downregulated genes in RNA-seq data from (A). Pathways with p value less than 0.05 are considered significant. The left side of each plot represents RDR1 group (R-WT), and the right side represents R-PE and RDR1-Mut (R-PE and R-Mut) groups.

(C) Scatterplot of gene expression in RNA-seq data from tumors of AAV-EGFP versus AAV-OsRDR1 group in A549 xenografts. Upregulated genes (FC > 2) are marked red, and downregulated genes (FC < 0.5) are marked blue. Downregulated RDR1-targeted cell-cycle genes are shown in yellow.

(D) Enrichment plots of GSEA of RNA-seq data from (C), using Reactome gene sets. Pathways with p value less than 0.05 are considered significant. The left side of each plot represents AAV-OsRDR1 group, and the right side represents AAV-EGFP group.